Boundary-Layer Meteorology (2005) 116:201–235
DOI 10.1007/s10546-004-2729-0

STABLE BOUNDARY-LAYER SCALING REGIMES: THE SHEBA DATA

ANDREY A. GRACHEV[1,2,3,*], CHRISTOPHER W. FAIRALL[2],
P. OLA G. PERSSON[1,2], EDGAR L. ANDREAS[4] PETER S. GUEST[5]
[1]*Cooperative Institute for Research in Environmental Sciences, University of Colorado Boulder, CO, U.S.A;* [2]*NOAA, Environmental Technology Laboratory, Boulder, CO, U.S.A;*
[3]*A.M. Obukhov Institute of Atmospheric Physics, Russian Academy of Sciences, Moscow, Russia;* [4]*U.S. Army Cold Regions Research and Engineering Laboratory, Hanover, NH, U.S.A;*
[5]*Naval Postgraduate School, Monterey, CA, U.S.A*

(Received in final form 20 March 2004)

Abstract. Turbulent and mean meteorological data collected at five levels on a 20-m tower over the Arctic pack ice during the Surface Heat Budget of the Arctic Ocean experiment (SHEBA) are analyzed to examine different regimes of the stable boundary layer (SBL). Eleven months of measurements during SHEBA cover a wide range of stability conditions, from the weakly unstable regime to very stable stratification. Scaling arguments and our analysis show that the SBL can be classified into four major regimes: (i) surface-layer scaling regime (weakly stable case), (ii) transition regime, (iii) turbulent Ekman layer, and (iv) intermittently turbulent Ekman layer (supercritical stable regime). These four regimes may be considered as the basic states of the traditional SBL. Sometimes these regimes, especially the last two, can be markedly perturbed by gravity waves, detached elevated turbulence ('upside down SBL'), and inertial oscillations. Traditional Monin–Obukhov similarity theory works well in the weakly stable regime. In the transition regime, Businger–Dyer formulations work if scaling variables are re-defined in terms of local fluxes, although stability function estimates expressed in these terms include more scatter compared to the surface-layer scaling. As stability increases, the near-surface turbulence is affected by the turning effects of the Coriolis force (the turbulent Ekman layer). In this regime, the surface layer, where the turbulence is continuous, may be very shallow (<5 m). Turbulent transfer near the critical Richardson number is characterized by small but still significant heat flux and negligible stress. The supercritical stable regime, where the Richardson number exceeds a critical value, is associated with collapsed turbulence and the strong influence of the earth's rotation even near the surface. In the limit of very strong stability, the stress is no longer a primary scaling parameter.

Keywords: Arctic, Coriolis effect, Ekman layer, Monin–Obukhov similarity theory, Richardson number, Stable boundary layer.

* Present address: Dr. Andrey Grachev, NOAA Environmental Technology Laboratory, R/ET6, 325 Broadway, Boulder, CO 80305-3328, U.S.A; Email: Andrey.Grachev@noaa.gov

1. Introduction

Determining momentum, heat, and mass exchange in the Arctic is a major challenge for modelling circulation in the Northern Hemisphere and global climate change. Understanding the atmospheric boundary layer and properly parameterizing the surface fluxes are of obvious relevance for climate modelling, weather forecasting, and other applications in the Arctic region. This study uses turbulence data collected over the Arctic pack ice during the Surface Heat Budget of the Arctic Ocean experiment (SHEBA) to examine different regimes of the stable boundary layer (SBL) in the atmosphere.

Although research has been done on the SBL for at least 50 years, a unified picture or theory does not exist. In some studies, the SBL has been classified into two separate regimes: the weakly stable boundary layer and the very stable boundary layer (see Mahrt, 1998; Mahrt et al., 1998). The weakly stable boundary layer is governed by traditional Monin–Obukhov similarity theory (MOST). In contrast, the very stable boundary layer is characterized by weak, intermittent turbulence even near the surface, and similarity theory appears to break down.

Over the past decade this two-regime view was questioned. Some investigators identified a transition regime between the weakly stable boundary layer and the very stable boundary layer. For example, Beyrich (1997) showed the vertical structure for three different types of SBL based on sodar measurements. Mahrt (1999) and Mahrt and Vickers (2002) also reviewed various features of the different stability regimes of the SBL. The very stable regime poses some of the most difficult questions in the SBL (Mahrt, 1999) because measurements are difficult (e.g., Howell and Sun, 1999), and the processes are very complex (e.g., intermittent turbulence, meandering motions, gravity waves, drainage flows).

Limited observations still remain a problem for SBL model validation. But observations in the Arctic offer several advantages for studying the structure of the SBL compared to measurements in the traditional nocturnal boundary layer in mid-latitudes. At high latitudes, especially during the polar night, long-lived SBLs can reach very stable states. The Arctic pack ice is also a rather uniform, flat surface without large-scale slopes and heterogeneity. Thus, the SHEBA data are not generally contaminated by drainage (katabatic) or strong local advective flows.

2. Description of the SHEBA Site and Instrumentation

Overviews of the SHEBA program and detailed descriptions of the site can be found in Andreas et al. (1999), Persson et al. (2002b), and Uttal et al.

(2002). Thus, only the relevant information about our SHEBA instruments and flux data will be given here.

The main SHEBA camp was deployed on the ice in the vicinity of the Canadian Coast Guard icebreaker *Des Groseilliers*, which was frozen into the Arctic ice pack north of Alaska from October 1997 to October 1998. During this period, the icebreaker drifted more than 2800 km in the Beaufort and Chukchi Seas, with coordinates varying from approximately 74° N and 144° W to 81° N and 166° W. The ship served as a floating research station providing accommodations and a logistics centre. The SHEBA research teams at the ice camp included the Atmospheric Surface Flux Group (ASFG, Andreas et al., 1999), which was responsible for direct measurement of the fluxes contributing to the surface energy balance.

The ASFG deployed a 20-m main micrometeorological tower, two short masts, and several other instruments on the sea ice 280–350 m from the *Des Groseilliers* at the northern edge of the main ice camp. The direction and distance of the tower from the ship and other obstacles varied during the year because the ice floe rotated and sheared apart. The ASFG site can be characterized as multi-year ice with summertime melt ponds and occasional nearby leads, with the closest being about 100 m in February and March. During the summer, as much as 22% of the ice in the intermediate area was covered by melt ponds (Perovich et al., 2002). At the height of summer, leads covered another 18% of the surface. The ASFG tower consisted of a 10-m-tall walk-up rectangular scaffold and a 20-m triangular section attached to the scaffold. This triangular section had two manual instrument carriages. The SHEBA ASFG tower was likely the largest meteorological tower ever placed on sea ice and the centrepiece of the SHEBA turbulence program.

The ASFG main tower collected turbulent and mean meteorological data at five levels, nominally 2.2, 3.2, 5.1, 8.9, and 18.2 m (or 14 m during most of the winter). Instruments at levels 2 ($z_2 \approx 3.2\,\mathrm{m}$), 3 ($z_3 \approx 5.1\,\mathrm{m}$), and 4 ($z_4 \approx 8.9\,\mathrm{m}$) were mounted on the scaffold. The instrument booms for level 1 ($z_1 \approx 2.2\,\mathrm{m}$) and 5 ($z_5 \approx 18.2$ or 14 m) were attached to the moveable carriages on the triangular section. During seven periods of 1–10 days each, the lower and upper levels, mounted on carriages, were moved to compare instruments between the tower levels.

The heights of the tower-mounted instruments above the snow or ice surface varied during the year because of snow accumulation and surface melt. The heights were obtained using the continuously measured snow depth and occasional manual height measurements. The range of heights for each of the five sensor levels can be found in Persson et al. (2002b, Table I).

Each level on the main tower had a Väisälä HMP-235 temperature and relative humidity (T/RH) probe and identical ATI (Applied Technologies, Inc.) three-axis sonic anemometer/thermometer. A sonic anemometer located at level 3 had some problems with electronics and the signal sometimes

contained irregular spikes. This anemometer was replaced in the end of February 1998. An Ophir fast-response infrared hygrometer was mounted on a 3-m boom at an intermediate level (about 8 m) just below level 4. The measurements used to determine the true orientation of the ASFG tower were made by an electronic compass located at the nearby Portable Automated Meteorological (PAM) station *Florida* on the same floe. Other instruments at the ASFG site are discussed in Andreas et al. (1999) and Persson et al. (2002b).

The sonic anemometers provided measurements of the three wind components (streamwise, u; cross-stream, v; and vertical, w) and sonic temperature (T_s) at five levels with a sampling rate of 10 Hz. Turbulent covariance values ($\langle u'w' \rangle$, $\langle v'w' \rangle$, $\langle w'T_s' \rangle$) and appropriate variances at each level are derived via eddy correlation based on 1 h averaging. Here $\langle\ \rangle$ is a time averaging operator, u, v, and w are the longitudinal, lateral, and vertical velocity components, respectively, and ($'$) denotes a fluctuation about the mean value, e.g., $u = \langle u \rangle + u'$. The sonic anemometers also provided measurements of the mean wind speed vector (magnitude and direction) at five levels.

The most commonly used method associated with a double rotation of the anemometer coordinate system is applied in the current study to compute u, v, and w. Rotation is needed to place the anemometer in the streamwise coordinate system. The first rotation sets $\langle v \rangle = 0$, and the second rotation sets $\langle w \rangle = 0$. Fast measurements of the specific humidity (q) were made by the Ophir hygrometer at 8.1 m at a sampling rate of 20 Hz. To match the sampling rate of the sonic anemometers, the data from the Ophir were pair-averaged to 10 Hz. The $\langle w'q' \rangle$ covariance was computed using w' derived from the level-4 sonic anemometer.

Momentum flux (τ), sensible heat flux (H_S), and latent heat flux (H_L) are derived from the measured covariance values according to

$$\tau = \rho u_*^2 = -\rho \langle u'w' \rangle, \tag{1}$$

$$H_S = c_p \rho \langle w'T' \rangle = c_p \rho (\langle w'T_s' \rangle - 0.51 T \langle w'q' \rangle), \tag{2}$$

$$H_L = (L_e + L_f) \rho \langle w'q' \rangle, \tag{3}$$

where u_* is the friction velocity, ρ the air density, T the air temperature, c_p the heat capacity of air at constant pressure, L_e and L_f in Equation (3) are the latent heats of vaporization and fusion respectively ($L_f/L_e \approx 0.13$).

Since the sonic anemometer measures the so-called 'sonic' virtual temperature, T_s, which is close to the virtual temperature, the moisture correction in (2) is necessary to obtain the correct sensible heat flux. That is, the temperature derived from the speed of sound measurements (sonic temperature), $T_s = T(1 + 0.51q)$, has the same form as the virtual temperature

$T_v = T(1 + 0.61q)$ (e.g. Kaimal and Gaynor, 1991; Larsen et al., 1993; Kaimal and Finnigan, 1994), and often T_s is referred to simply as the virtual temperature. The error involved in assuming $T_s \approx T_v$ is on the order of 0.01K (Kaimal and Gaynor, 1991), well within the bounds of our other temperature measurement uncertainties.

During SHEBA, the data recovery for the covariance $\langle w'q' \rangle$ was significantly less than for the covariance $\langle w'T_s' \rangle$ (Persson et al., 2002b, Figure 4a and b). The processed H_S in the dataset are computed using the covariance $\langle w'q' \rangle$ when available and bulk estimates of H_L when not. However, the moisture correction term in Equation (2) is usually small for Arctic conditions, $0.51T\frac{\langle w'q' \rangle}{\langle w'T_s' \rangle} = \left(1 + \frac{L_e + L_f}{0.51 c_p T} Bo\right)^{-1} < 0.06$, where the Bowen number $Bo = H_S/H_L > 1$ for $T < 0\,^{\circ}\mathrm{C}$ (Andreas and Cash, 1996). A large summertime latent heat flux of 10 W m^{-2} would imply an overestimation of only 0.5 W m^{-2} for H_S. During most of the year, the error is much less, and therefore $\langle w'T_s' \rangle \approx \langle w'T_v' \rangle \approx \langle w'T' \rangle$. However, in the present study, the distinction among T_s, T_v and T is retained for hourly flux calculation, and the true Equation (2) is used.

Several data-quality indicators based on objective and subjective methods have been applied to the original flux data. Flux data have been edited for unfavourable relative wind direction for which the tower was upwind of the sonic anemometers. However, wind speeds and direction for these times have not been removed since they are still useful in describing the climatology of the site. Because of the careful way we arranged the ice camp, the wind blew from disturbed areas only about 10% of the time. Most of the station structures and the *Des Groseilliers* itself were located within these sectors.

Some other quality-control criteria are based on validity limits for the streamwise and vertical-velocity variances. In post-processing, we corrected and edited the flux time series. We examined 1-h spectra and cospectra to filter noise (i.e., reject spikes) that were probably due to tower vibrations. To separate the gravity-wave and turbulent portions of the spectra, we partitioned the wind stress and heat flux into low- and high-frequency components defined by integrating the cospectra from 0 to f_L and from f_L to 5 Hz (the Nyquist frequency). The frequency f_L is the sixth spectral value (0.0061 Hz, or a period of about 2 min). This value is close to the cutoff frequency 0.01 s^{-1} used by Forrer and Rotach (1997). The total flux is the sum of low- and high-frequency components. We also computed the turbulent flux appropriate in MOST by neglecting the low-frequency part for those cases when the low part of uw cospectra was positive. These fluxes are used in the current study.

The 'slow' temperature and humidity probes provided air temperature and relative-humidity measurements at five levels. Instantaneous temperature/relative humidity and other slow data (e.g., shortwave and longwave radia-

tion, surface temperature) were collected by Campbell dataloggers with 5-s sampling intervals. The Campbells then averaged these raw values to 1-min means in real time. The 1-min values were used to compute the 10-min statistics (means and standard deviations). In post-processing, the 10-min means were used to produce hourly averages.

Measuring the surface temperature, T_S, is important for both parameterizing fluxes and understanding the energy balance in the surface layer. However, measuring T_S accurately is difficult. Three different methods were used to estimate T_S at the ASFG site: Eppley pyrgeometers, a Barnes PRT-5 precision radiation thermometer, and a General Eastern dew-point hygrometer (Claffey et al., 1999). Our best estimates of T_S are principally based on slight corrections to the Eppley radiometer temperatures. When the Eppley data were known to be wrong, we used the Barnes radiometer temperatures. Other details of the 'fast' and 'slow' data processing, accuracy, and calibration can be found in Persson et al. (2002b).

The main SHEBA tower was instrumented for over 8,000 h. Well over 6,000 h of that period yielded useful data. Apparently, the flux-profile data we report here constitute the largest single turbulent dataset ever collected in the atmospheric surface layer.

3. Surface Layer Conditions during SHEBA

Persson et al. (1999, 2002b) described the near-surface environmental conditions and the surface energy balance in detail. Therefore, we give only a brief sketch of the near-surface conditions here.

The sunless ('dark') period (or polar night) at the SHEBA site began on 12 November 1997 and lasted 83 days until 29 January 1998 (Julian days 312–394, starting from 1 January 1997). Daily average wintertime (December–February) air temperatures ranged between −40 °C and −19 °C (Andreas et al., 2002), but temperatures underwent frequent, rapid transitions due to the occurrence of low clouds (Persson et al., 1999). The minimum hourly-averaged surface temperature was −44.1 °C.

According to the analysis of Persson et al. (2002b), the temperatures at SHEBA were typical of most previous climatological estimates and observations through most of the year. However, during the spring (March–April), temperatures were 3–8 °C above normal. The summer melt season started on 29 May and ended between 14 and 22 August (i.e., 77–85 days long). The melt season is characterized by surface and air temperatures that are nearly constant at 0 °C. The SHEBA melt season was longer than observed during previous studies (e.g., at the Soviet drifting ice stations deployed in 1950–1990; e.g., Yanes, 1962) principally because of an early onset (Persson et al., 2002b). The humidity was close to saturation with

respect to ice throughout the year, with slight supersaturation during the winter and subsaturation during the summer (Andreas et al., 2002; Persson et al., 2002b).

The winds were strongest in the winter and weakest in the summer. The maximum hourly averaged wind speed was 16 m s^{-1}. The most frequent true wind directions during the entire year were from 40°–120°, with strongest winds, averaging 6–7 m s^{-1}, coming from true east. The winds tended to be easterly in the spring and fall, northerly in the winter, and southerly in the summer. Systematic seasonal variations in wind speed and wind direction were likely due to a combination of true seasonal variations and spatial variations along the drift track of the SHEBA ice camp.

Monthly averages of hourly air temperatures and the incoming solar radiation show large diurnal variations during spring (Persson et al., 2002b). During the sunless period, the diurnal cycle of insolation is absent, although some diurnal oscillations of the temperature and the wind field may be the result of the solar tides (cf. Dabberdt, 1970).

Monthly mean temperature profile measurements show that the near-surface environment is strongly stable during the six winter months (November–April) and near neutral or only weakly stratified during the other months. However, closer examination of the 1-h data shows that near-neutral conditions are also very common during the winter. These winter well-mixed conditions occur with clouds and higher wind speeds. The occurrence of weak stable stratification is fairly common during the summer, when the surface temperature is constant at 0 °C and warm air is advected over the site. The monthly mean temperature profiles show that, from November through April, an inversion is present in the lowest 15 m of the atmosphere over pack ice. The inversion strength is a maximum in December. The vertical gradient decreases after the sun rises in early February, and in May the vertical thermal structure reverses. The mean vertical divergence of turbulent sensible heat flux in the surface layer produces atmospheric cooling during the winter and warming during the summer (Persson et al., 1999, 2002b).

4. Stratified Atmospheric Boundary Layer

Monin–Obukhov similarity theory (Obukhov, 1946; Monin and Obukhov, 1954), or surface-layer scaling, is the commonly accepted approach to describe the near-surface atmospheric layer. According to MOST, properly scaled dimensionless characteristics of the turbulence at reference height z are universal functions of a stability parameter, $\zeta \equiv z/L$, where

$$L = -\frac{u_*^3 T_v}{\kappa g \langle w' T_v' \rangle} \tag{4}$$

is the Obukhov length (κ is the von Karman constant, and g is the acceleration due to gravity). The friction velocity in Equation (4) is computed according to Equation (1). It should be noted that Equation (4) is based on the surface fluxes of momentum and buoyancy. According to MOST, the vertical gradients of mean wind speed and temperature are assumed to be

$$\frac{dU}{dz} = \frac{u_*}{\kappa z}\varphi_{\mathrm{m}}(z/L), \tag{5a}$$

$$\frac{d\theta}{dz} = \frac{T_*}{\kappa z}\varphi_{\mathrm{h}}(z/L), \tag{5b}$$

where $T_* = -\langle w'T'\rangle/u_*$ is the temperature scale and $\varphi_{\mathrm{m}}(z/L)$ and $\varphi_{\mathrm{h}}(z/L)$ are non-dimensional universal functions ('stability functions') for velocity and potential temperature (θ) gradient, respectively. In this study, we use the traditional value of $\kappa = 0.40$ for both wind speed and temperature profiles Equation (5).

Another widely used indicator of stability is the Richardson number. The flux Richardson number, *Rf*, and the gradient Richardson number, *Ri*, are defined by

$$Rf = \frac{g}{T_{\mathrm{v}}}\frac{\langle w'T_{\mathrm{v}}'\rangle}{\langle u'w'\rangle(dU/dz)} \equiv \frac{z/L}{\varphi_{\mathrm{m}}}, \tag{6a}$$

$$Ri = \frac{g}{T_{\mathrm{v}}}\frac{d\theta_{\mathrm{v}}/dz}{(dU/dz)^2}. \tag{6b}$$

Close to the surface, it is convenient to introduce a bulk Richardson number:

$$Ri_{\mathrm{B}} = -\frac{gz}{T_{\mathrm{v}}}\frac{\Delta\theta + 0.61T_{\mathrm{v}}\Delta q}{U^2}, \tag{7}$$

where $\Delta\theta$ and Δq are differences in the potential temperature and the specific humidity between the surface and reference level z.

In the strong stability limit ($\zeta \gg 1$), MOST predicts that various quantities become independent of z. Thus, z is no longer a primary scaling variable and $\varphi_{\mathrm{m}} \propto \varphi_{\mathrm{h}} \propto \zeta$ (Obukhov, 1946; Monin and Obukhov, 1954). This is because vertical motion is inhibited by the stable stratification, and the turbulence no longer communicates significantly with the surface (Monin and Yaglom, 1971). This was termed 'z-less stratification' by Wyngaard and Cotè (1972) and Wyngaard (1973).

A simple linear interpolation $\varphi_{\mathrm{m}} = \varphi_{\mathrm{h}} = 1 + \beta\zeta$, where β is a constant, has been suggested to provide blending between neutral and very stable ('z-less') cases (e.g. Zilitinkevich and Chalikov, 1968; Webb, 1970). Note that these forms for φ_{m} and φ_{h} also agree with the linear approximation of their expansion in a power series for fairly small values of ζ (log-linear profiles). The linear equations for φ_{m} and φ_{h} in stable conditions fit the available

experimental data well for $\zeta < 1$ (Businger et al., 1971; Dyer, 1974; Yaglom, 1977; Dyer and Bradley, 1982; Högström, 1988; King, 1990; Garratt, 1992; Howell and Sun, 1999). Traditionally the linear equations in the stable case together with the formulas for φ_m and φ_h in the unstable case are called the Businger–Dyer relations (Businger, 1966; Dyer and Hicks, 1970; Businger et al., 1971; Dyer, 1974; Dyer and Bradley, 1982; Businger, 1988).

However, the stability functions increase more slowly in very stable conditions than predicted by the log-linear law and moreover φ_h tends to level off (Howell and Sun, 1999; Forrer and Rotach, 1997; Yagüe et al., 2001). This suggests that z-less scaling is not applicable under such conditions. Recently, based on the analysis of the standard deviations and dissipation rates covering almost five orders of magnitude in ζ, Pahlow et al. (2001) found that the concept of z-less stratification does not hold in general.

We must make one additional remark regarding the paper by Yagüe et al. (2001). From a study of the SBL overlying an Antarctic ice shelf, Yagüe et al. (2001) found that in the very stable conditions the non-dimensional gradients φ_m and φ_h reach a constant value (i.e., become independent of ζ). This was interpreted as a validity of the z-less approach (Ibid., pp. 205, 215, 221). The concept of z-less stratification actually predicts that the *dimensional gradients*, Equation (5), become independent of z, which corresponds to $\varphi_m \propto \varphi_h \propto \zeta$ (e.g. Wyngaard and Cotè, 1972, their Equation (2)). Thus, the data presented by Yagüe et al. (2001) in fact indicate that z-less scaling is not valid in general.

Mahrt and Vickers (2002) defined the traditional boundary layer or surface-flux dominated SBL, where turbulence is generated by surface roughness, and momentum and heat fluxes are about constant or decrease monotonically with height. Thus, z is still important and the z-less concept is not applicable in this case. Accordingly, non-traditional boundary-layer scaling methods are associated with z-less stratification and an upside-down boundary layer, in which turbulence is generated primarily at the top of the boundary layer. In the upside-down boundary layer, the turbulence source is detached from the surface and generated by shear usually associated with a low-level jet (Smedman, 1988; Mahrt, 1999; Mahrt and Vickers, 2002). In this case, turbulence increases with height and the transport of the turbulent kinetic energy is downward.

As discussed above, the traditional SBL is classified into several separate regimes: the weakly stable boundary layer, an intermediate (or transition) regime, and the very stable boundary layer. Traditional MOST works well in the weakly stable boundary layer. In contrast, the very stable boundary layer is characterized by weak, intermittent turbulence even near the surface (e.g., Holtslag and Nieuwstadt, 1986), and it has been suggested that similarity theory breaks down. In the transition regime, the approximation of height-independent fluxes underlying MOST is invalid. However, MOST can be restored in the form of local scaling if L (Equation 4) is replaced by Λ, where Λ is the local Obukhov length based on the local fluxes at height z rather than

on the surface values (Nieuwstadt, 1984; Holtslag and Nieuwstadt, 1986; Sorbjan, 1989). Mahrt et al. (1998) found for a fixed level $z = 10\,\mathrm{m}$ that the weakly stable regime corresponds to $0 < \zeta < 0.06$, and the very stable regime is associated with $\zeta > O(1)$.

The formation of an Ekman spiral indicates that the near-surface turbulence is affected by both the Coriolis parameter and the Brunt–Väisälä frequency of the outer flow (non-local scaling parameters) as well as by the shear stress and the buoyancy flux (local scaling parameters). This state can be treated as a non-local scaling regime, since a functional dependence on z/h, where h is the SBL depth, applies at all levels (Holtslag and Nieuwstadt, 1986; Mahrt, 1999). Zilitinkevich and Calanca (2000) and Zilitinkevich (2002) derived a non-local theory for the SBL without the effect of the Earth's rotation.

In the next section we consider the traditional boundary-layer regimes. Note, however, that classifying the SBL into a few states is probably an oversimplification.

5. SBL Regimes in the Arctic

Our eleven months of measurements during SHEBA cover a range of stability conditions, from the weakly unstable regime to the very stable stratification of the prevailing SBL during winter. These long-term, multi-level observations of the SBL allow us to consider different SBL regimes in detail.

5.1. Weakly stable case

In the weakly stable boundary layer, the downward heat flux initially increases with increasing ζ. Derbyshire (1990), however, predicted that the downward heat flux eventually reaches a maximum then decreases with increasing ζ (cf. Jordan et al., 1999). Malhi (1995) found that the maximum downward heat flux occurs at $\zeta = 0.2$. According to Mahrt et al. (1998), this maximum occurs at roughly $\zeta = 0.06$ for their 10-m data and occurs at roughly $\zeta = 0.02$ for their 3-m data. Pahlow et al. (2001) also found a height dependence for the maximum of the downward heat flux. The maximum of the downward heat flux defines the ζ boundary between the weakly stable and transition regimes (Mahrt et al., 1998).

The sensible heat flux, H_S, observed during SHEBA at five levels is shown in Figure 1 as a function of $\zeta_1 = z_1/L_1$ and z/Λ. Hereinafter, z/Λ refers to a local stability parameter at levels 1–5 defined as $z/\Lambda \equiv z_n/L_n \equiv \zeta_n$ ($n = 1 - 5$); whereas z/L refers to the surface stability parameter associated with fluxes measured at the level 1. That is, $\zeta = z/L \equiv z_n/L_1$ ($n = 1 - 5$). The data in Figure 1 are based on individual 1-h averages further averaged in four logarithmically spaced stability bins within each decade in stability. Similar plots for the individual 1-h points can be found in Grachev et al. (2002).

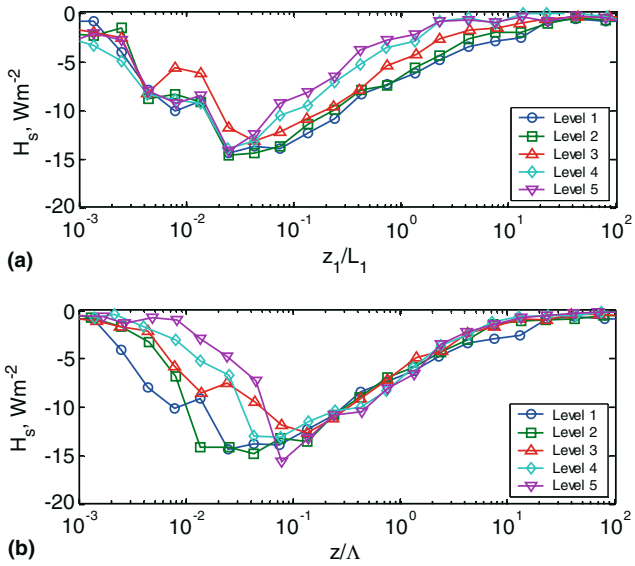

Figure 1. Bin-averaged sensible heat flux (medians), H_S, measured at five levels versus (a) the stability parameter at level 1, z_1/L_1 and (b) a local stability parameter, $z/\Lambda \equiv z_n/L_n$ ($n = 1-5$) during the 11 months of measurements. Data with a temperature difference between the air (at median level) and the snow surface of less than 0.5 °C were rejected because of the large uncertainty in determining the sensible heat flux in such conditions.

According to Figure 1a, the maximum of the observed downward heat flux at all levels (except level 3) occurs at $\zeta_1 \approx 0.025$. However, when we use local scaling, the maximum is a function of z/Λ (Figure 1b). The downward heat flux reaches a maximum at roughly $z/\Lambda \approx 0.02$ for the level 1 ($\approx$2.2 m) data and at roughly $z/\Lambda \approx 0.1$ for the level 5 ($\approx$18.2 or 14 m) data. The maximum heat flux at levels 2 and 4 occurs at values of z/Λ located sequentially between the values for levels 1 and 5. This dependence on the measurement height is consistent with the results reported by Mahrt et al. (1998). The above z/Λ values correspond to bulk Richardson numbers of $Ri_B \approx 0.004$ and $Ri_B \approx 0.01$ for levels 1 and 5, respectively.

Because Figure 1a is plotted in coordinates of H_S versus $\zeta_1 = z_1/L_1$ (i.e. a stability parameter with fixed z), it also shows that H_S at all levels (except level 3) is about constant for weakly stable conditions. With increasing stability, however, the downward heat flux at lower levels is systematically greater than the flux at higher levels (Figure 1a). Plotting in the log-linear coordinates H_S versus $\log(z/\Lambda)$ (Figure 1b), or H_S versus $\log(z/L)$ (not shown), discloses that all curves collapse to a single straight line shows that the sensible heat flux decreases with height as a logarithmic function for $0.2 \lesssim z/\Lambda \lesssim 4$.

Note that the dependence of $T_* = -\langle w'T' \rangle / u_*$ on stability is similar to H_S in Figure 1 but with the opposite sign since $T_* > 0$ in stable conditions

(Grachev et al., 2003). In the near-neutral case, $T_* \to 0$ since $\langle w'T' \rangle \approx 0$ and $u_* \neq 0$. With further increasing stability, T_* increases and reaches a maximum; $T_* \to 0$ in the very stable case. The last result is not trivial since both $\langle w'T' \rangle \to 0$ and $u_* \to 0$ as ζ (or Ri_B) $\to \infty$.

With further increasing stability, the downward heat flux, the drag coefficient, and the turbulence intensity decrease rapidly because negative buoyancy inhibits vertical transfer. However, the regime where the turbulent fluxes are constant with height extends slightly beyond the point where H_S reaches its maximum magnitude. Using our SHEBA data, we tested the assumption underlying MOST that the turbulent fluxes are constant with height. Seasonal variations of the vertical flux divergence during SHEBA have been considered by Guest et al. (1999). The greatest vertical flux deviations occurred in the winter (mostly highly stable situations); the smallest occured in the spring. However, according to Guest et al. (1999), the constant flux assumption required for MOST was reasonably accurate for much of the SHEBA observation period, even with the presence of open water within 2 km of the tower and large variations in the surface roughness due to ridges and other features in the upwind fetch.

Figure 2a shows the difference of the streamwise stress τ_n measured at a level z_n and the stress τ_{n+1} measured at a level z_{n+1} normalized by τ_n as a function of $\zeta_{n+1} \equiv z_{n+1}/L_{n+1}$, which is z/Λ at a level z_{n+1} $(n = 1 - 4)$. A similar plot for the sensible heat flux is shown in Figure 2b. To reduce a

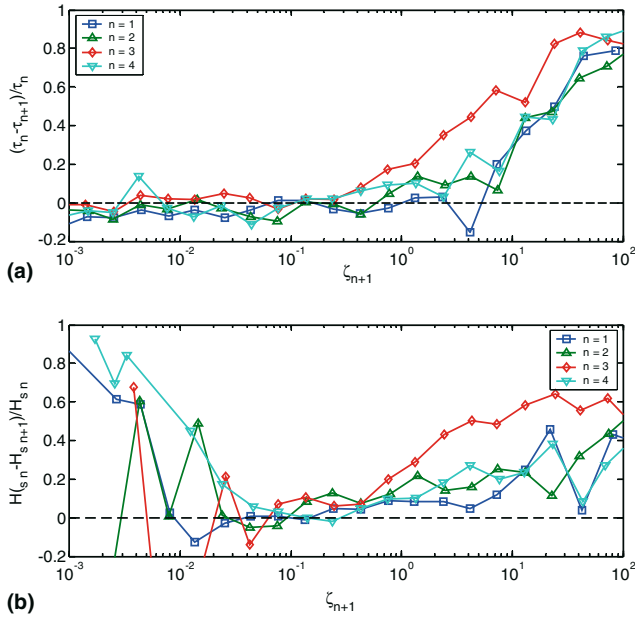

Figure 2. Vertical divergence of (a) the downwind stress and (b) the sensible heat flux plotted for period from 31 October 1997 (JD 304) until 21 March 1998 (JD 445).

possible side effect on the fluxes associated with the inhomogeneity in the surface temperature, we plot Figure 2 only for the period from 31 October 1997 (JD 304) until 21 March 1998 (JD 445, vernal equinox). During this winter period the floe around the tower is more or less compact and totally snow covered and the surface is more homogeneous in temperature than during the melting period (see Section 5.3).

Individual measurements of both τ and H_S typically have uncertainties of $\pm 20\%$. That is, with τ as an example, for the divergences plotted in Figure 2, the uncertainty propagates as

$$\frac{|\tau_n(\pm 20\%/\sqrt{N})| - |\tau_{n+1}(\pm 20\%/\sqrt{N})|}{|\tau_n(\pm 20\%/\sqrt{N})|} = 1 - \frac{|\tau_{n+1}(\pm 20\%/\sqrt{N})|}{|\tau_n(\pm 20\%/\sqrt{N})|}$$
$$= 1 - 1(\pm 40\%/\sqrt{N}),$$

if we assume that τ is really independent of height. Here also, N is the number of hourly values used to compute the averages. According to our data, N within a bin increases from 10 to 20 at $z/\Lambda \approx 0.001$ to ≈ 100 at $z/\Lambda \approx 0.1$, and then falls to 10–20 at $z/\Lambda \approx 100$. Clearly, with our measurement accuracy, we must assume that τ_n and τ_{n+1} are, on average, the same if the ratios plotted in Figure 2a are smaller than $0.4/\sqrt{N} \approx 0.04 - 0.1$. A similar argument holds for the heat fluxes plotted in Figure 2b.

According to Figure 2, for z/Λ less than about 0.1, the momentum flux and the sensible heat flux may be considered independent of height (on average). The greater scatter of points in Figure 2b for $z/\Lambda \lesssim 0.05$ is associated with the relatively small sensible heat flux and unreliable measurements in near-neutral conditions. Thus, a regime for $0 < z/\Lambda \lesssim 0.1$ (or $0 < \zeta \lesssim 0.1$) may be identified as the surface-layer scaling regime or the weakly stable case (cf. Mahrt et al., 1998). Traditional surface-layer scaling (MOST) works well in this regime (see next section). Independent flux measurements at the SHEBA ice camp made by Duynkerke and de Roode (2001) in May 1998 also show that the observed stable boundary layer above sea ice may be, on average, characterized as weakly stable during the measurement period.

5.2. Transition regime

According to Figure 2, the assumption of height-independent fluxes becomes invalid for $\zeta \approx z/\Lambda \gtrsim 0.1$. Figure 3 shows typical cospectra for the momentum and sonic temperature fluxes, respectively, at the five levels where $z/\Lambda \gtrsim 0.1$. According to Figure 3, the magnitudes of the stress and the sensible heat flux decrease with increasing height. Although z/Λ (or ζ) also increases with increasing height, the surface-generated wind shear is large enough to maintain turbulence at all five sonic levels in this regime. Note that the fluxes at levels 1 and 2 in both Figure 3a and b are approximately the same.

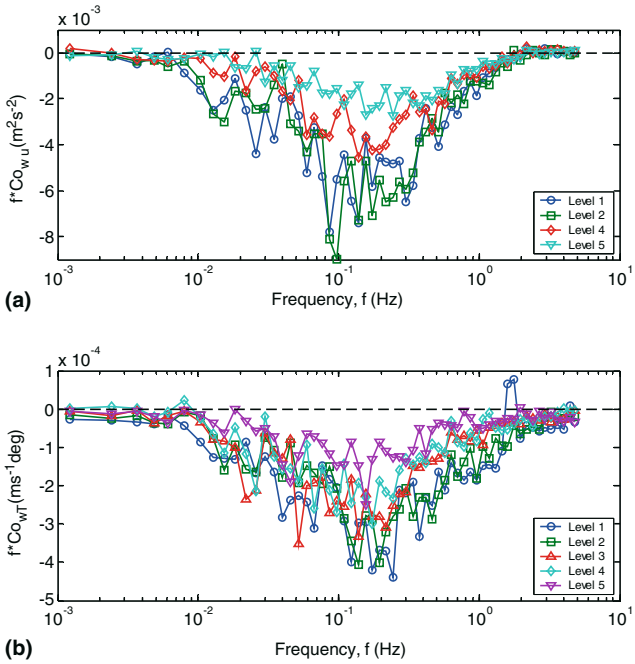

Figure 3. Typical (a) stress cospectra at four levels (level 3 is missing) in the transitional local-scaling regime (1998 JD 45.4167), and cospectra of the sonic temperature flux at the five levels in the transitional local-scaling regime (JD 324.5833 in 1997). In the upper panel (a), u_*, decreases with increasing height: $u_{*1} \approx 0.134\,\mathrm{m\ s^{-1}}$, $u_{*2} \approx 0.134\,\mathrm{m\ s^{-1}}$, $u_{*4} \approx 0.100\,\mathrm{m\ s^{-1}}$ and $u_{*5} \approx 0.080\,\mathrm{m\ s^{-1}}$, (levels 1, 2, 4 and 5). Stability parameter increases with increasing height: $\zeta_1 \approx 0.128$, $\zeta_2 \approx 0.173$, $\zeta_4 \approx 0.697$ and $\zeta_5 \approx 1.893$. Wind direction, α, is about constant with height: $\alpha_1 \approx 16°$, $\alpha_2 \approx 12°$, $\alpha_4 \approx 16°$ and $\alpha_5 \approx 18°$. In the bottom panel (b) downward sensible heat flux, H_S, decreases with increasing height: $H_{S1} \approx -1.66\,\mathrm{W\ m^{-2}}$, $H_{S2} \approx -1.44\,\mathrm{W\ m^{-2}}$, $H_{S3} \approx -1.20\,\mathrm{W\ m^{-2}}$, $H_{S4} \approx -0.96\,\mathrm{W\ m^{-2}}$ and $H_{S5} \approx -0.64\,\mathrm{W\ m^{-2}}$ (level 1–5). Stability parameter, z/Λ, increases with increasing height: $\zeta_1 \approx 0.096$, $\zeta_2 \approx 0.102$, $\zeta_3 \approx 0.122$, $\zeta_4 \approx 0.300$, and $\zeta_5 \approx 0.533$. Wind direction, α, is about the same for all five levels: $\alpha_1 \approx 136°$, $\alpha_2 \approx 138°$, $\alpha_3 \approx 141°$, $\alpha_4 \approx 138°$ and $\alpha_5 \approx 139°$.

Previous studies showed that in this regime MOST seems adequate, but similarity theory should be re-defined in terms of local similarity in which the Obukhov length is based on the local fluxes at height z (Wyngaard, 1973; Nieuwstadt, 1984; Holtslag and Nieuwstadt, 1986). For this reason, this regime may be considered as a local-scaling regime (or transition regime; cf. Mahrt, 1999). Using data collected over the Greenland ice sheet, Forrer and Rotach (1997) showed that local scaling is superior to surface-layer scaling in this regime. Using mid-latitude nocturnal boundary-layer observations, Howell and Sun (1999) corroborated this result.

The non-dimensional gradients of the wind speed (φ_m) and temperature (φ_h) defined by Equation (5) for the SHEBA data are presented in Figures 4

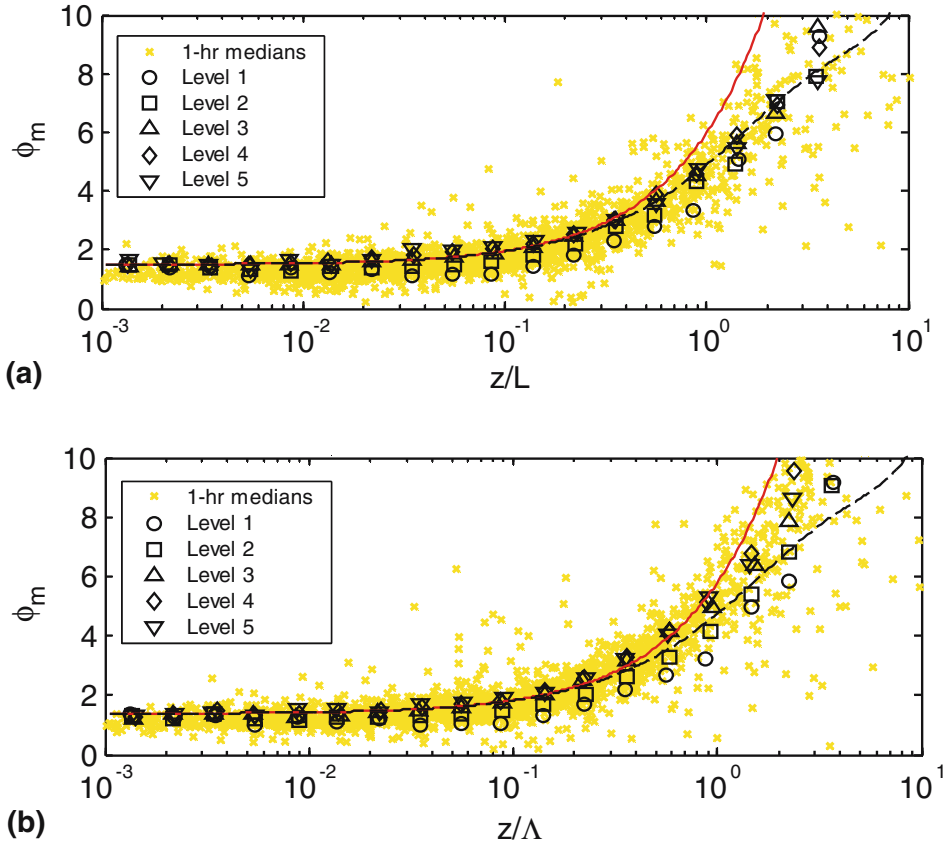

Figure 4. Plots of the bin-averaged non-dimensional velocity gradient, φ_m, (medians) against (a) the surface MOST stability parameter, z/L and (b) the local MOST stability parameter, z/Λ, for levels 1–5 during the 11 months of measurements. The solid curves represent the Businger–Dyer relationship, $\varphi_m = \varphi_h = 1 + \beta\zeta$ with $\beta = 5$, and the dashed ones are based on the Beljaars and Holtslag (1991) formulae. Functions φ_m , φ_h and the Obukhov length in the upper panel (a) are based on the fluxes measured at level 1 ('surface fluxes'), whereas φ_m, φ_h, and Λ in the bottom panel (b) are based on the local fluxes. Individual 1-h averaged data based on the median fluxes for the five levels are shown as background symbols.

and 5. These functions are plotted in the log-linear coordinates for z/L and $z/\Lambda \leq 10$ to focus on the φ_m and φ_h behaviour in the considered regime. The stability functions in the limit of very strong stability are discussed in Section 5.4. The bin-averaged data from each measurement level in Figures 4 and 5 are indicated by different symbols. The individual 1-h averaged data based on the median fluxes and other medians (heights, temperatures, etc.) for the five levels are also shown in Figures 4 and 5 as background symbols. These points give an estimate of the available data at one level and the typical scatter of the data. The median fluxes are computed from the median cospectra (i.e., at

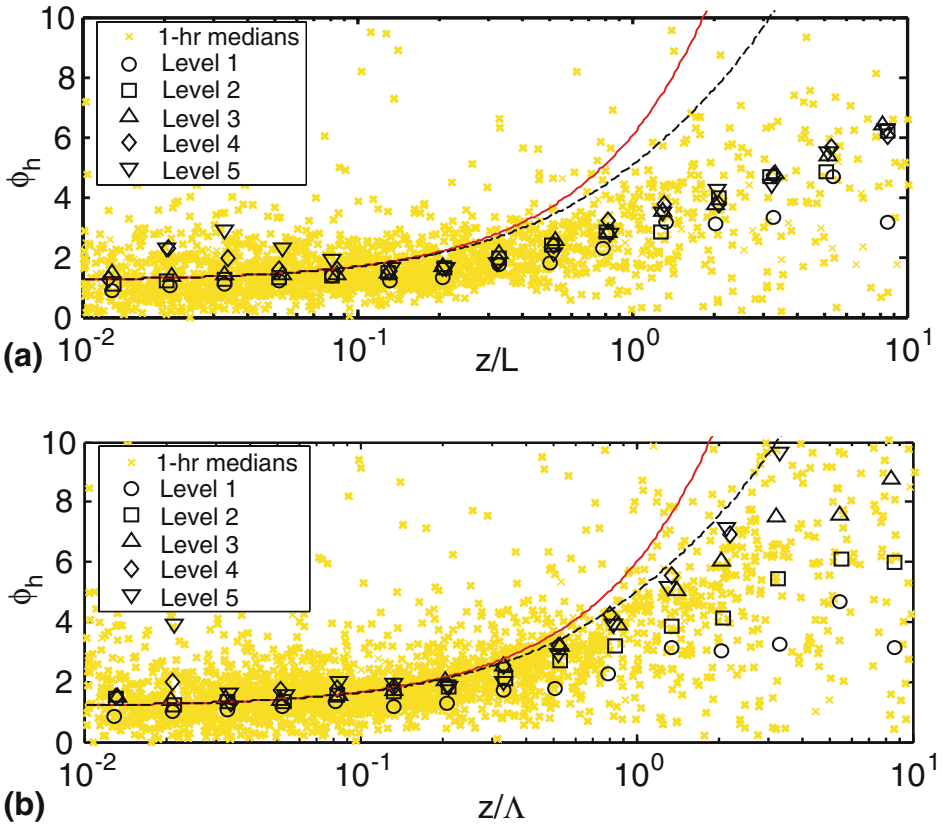

Figure 5. Same as Figure 4 but for the non-dimensional temperature gradient, φ_h. Data with the temperature difference between the air (at median level) and the snow surface less than 0.5° have been rejected to avoid the large uncertainty in determining the sensible heat flux.

each frequency a median is computed from the values at the heights where data are available).

Figures 4a and 5a are based on MOST scaling, Equation (4), and Figures 4b and 5b show φ_m and φ_h as functions of the local scaling, z/Λ. The solid curves in Figures 4 and 5 represent the Businger–Dyer expressions, $\varphi_m = \varphi_h = 1 + \beta\zeta$ with $\beta = 5$. The dashed curves are based on the relationships proposed by Beljaars and Holtslag (1991).

The vertical wind and temperature gradients in Equation (5) were obtained by fitting the following second-order polynomial through the 1-h profiles:

$$x(z) = p_1(\ln z)^2 + p_2 \ln z + p_3. \tag{8}$$

Here $x(z)$ represents either the wind speed, U, or the potential temperature, θ, at measurement level z. At least three levels with good data have been used for the interpolation of the wind speed and temperature profiles from Equation (8). The gradients were determined by evaluating the derivative of Equation (8) with

respect to z for any levels 1–5 where good turbulence measurements existed; then the functions φ_m and φ_h were evaluated at these levels.

According to Figures 4 and 5, the φ_h estimates include more scatter than the φ_m estimates. Our SHEBA data also show that using surface scaling, z/L, instead of local scaling, z/Λ, leads to less scatter between different observations levels for both φ_m and φ_h, especially for cases of strong stability. This may indicate that the observed SBL was controlled by the surface fluxes.

Figures 4 and 5 show that data for both φ_m and φ_h obtained at levels 3–5 ($z \sim O(10\,m)$) collapse to a single curve over a wide range of z/L better than the data obtained at levels 1 and 2 ($z \sim O(2\,m)$). The data for levels 1 and 2 are systematically lower than the data at higher levels beginning with $z/L \gtrsim 0.03$ for φ_m (Figure 4) and $z/L \gtrsim 0.5$ for φ_h (Figure 5). This bias may be because levels 1 and 2 are located too close to the surface. According to Mahrt (1999), close to the surface the influence of individual roughness elements and surface heterogeneity in very stable conditions is more pronounced, since vertical mixing is weak and characterized by small eddies (see also the discussion in Section 5.3). Therefore, the surface heterogeneity modifies the local turbulence field on the vertical scale of the heterogeneity elements (e.g., meltponds), and distortion of φ_m and φ_h near the surface may be substantial. Another reason for the bias may be associated with observational problems in very stable conditions. Howell and Sun (1999) demonstrated that sonic anemometers in the SBL may miss some fraction of the small-scale flux at lower heights even if data are collected at 10 samples per second (see also Kaimal and Finnigan (1994, p. 219)).

According to Figures 4a and 5a, the SHEBA observations agree reasonably well with the Businger–Dyer expressions (MOST predictions) for $0 < \zeta \lesssim 0.1$. For φ_m, the agreement is reasonable up to $\zeta \approx 0.3$ (Figure 4a). With further increasing stability, φ_m tends to follow the Beljaars–Holtslag functions rather than the Businger–Dyer formulae (Figure 4a). Of course, the Businger–Dyer formulae were never intended to apply in very stable conditions. Our estimates of φ_h for $\zeta \gtrsim 0.1$ are smaller than the φ_h derived from both the Beljaars–Holtslag and Businger–Dyer relations (Figure 5a).

Both stability functions φ_m and φ_h expressed with local scaling (Figures 4b and 5b) show better fits with the MOST predictions (Businger–Dyer formulae) than those expressed with surface-layer scaling (Figures 4a and 5a). The stability function φ_m is in good agreement with MOST for $z/\Lambda \lesssim 1$ (Figure 4b), while φ_h fits the Businger–Dyer expression reasonably well for $z/\Lambda \lesssim 0.3$ and the Beljaars–Holtslag relationship for $z/\Lambda \lesssim 1$ (Figure 5b). For this reason, this regime may be treated as a local-scaling regime. Again, this conclusion is valid for the data obtained at levels 3–5. Figure 5b shows significant systematic divergence of φ_h measured at the different levels (especially near surface) for $z/\Lambda \gtrsim 0.5$, whereas such strong divergence is not observed for φ_m (Figure 4b). This difference may indicate the importance of the radiative flux

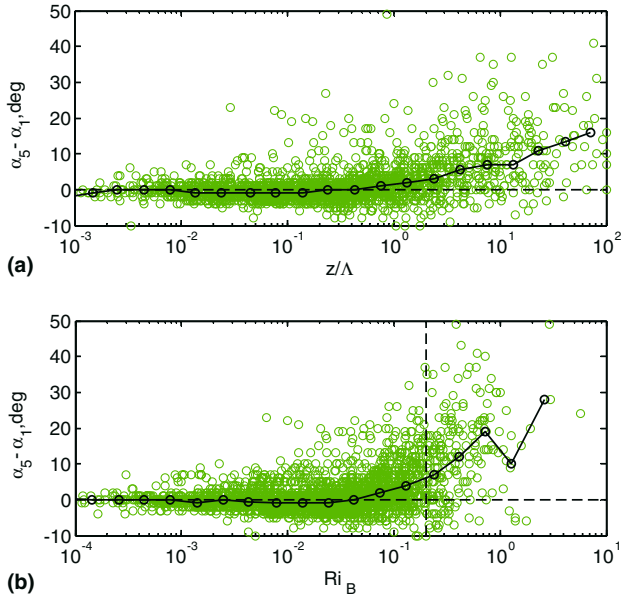

Figure 6. Difference between wind direction at levels 5 and 1 (individual 1-h averaged data and bin-averaged medians) as function of (a) z/Λ (at level 5) and (b) Ri_B (level 5 minus surface values). The vertical dashed line in the bottom panel corresponds to a critical Richardson number, Ri_B, of 0.2.

divergence, which may produce significant effects on the near-surface temperature gradient (e.g., Garratt and Brost, 1981; Duynkerke, 1990).

In the transition regime, the surface layer is not affected by the turning effects of the Coriolis force, and the direction of the wind is approximately constant at all five levels (see captions to Figure 3). The upper limit for the transition regime may be defined as the height where the assumption of a constant wind direction fails. Figure 6 shows the difference between wind directions measured at levels 5 and 1, $\alpha_5 - \alpha_1$, as a function of z/Λ and Ri_B (the angle resolution is 1°). The bulk Richardson number in Figure 6b is based on Equation (7). The observed angles show that the turning (Ekman-type spiral) cannot be neglected for $z/\Lambda \gtrsim 1$ and $Ri_B \gtrsim 0.07$. We obtained a similar result for the difference $\alpha_4 - \alpha_1$, but wind direction differences for the lower levels are not reliable as the sensors were too close to one another.

The increase in wind turning with increasing stability results from reduced frictional effects. The ratio of the friction force and the Coriolis force is called the Ekman number, Ek. The Ekman number, which is non-dimensional, can be specified in several different ways. For atmospheric observations, it is convenient to define Ek through the standard surface-layer parameters:

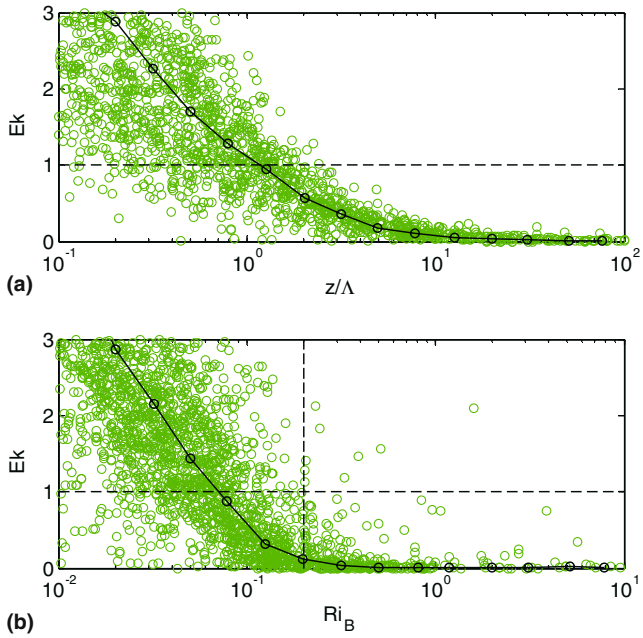

Figure 7. Dependence of the Ekman number (9) measured at level 5 (individual 1-h averaged data and bin-averaged medians) as functions of (a) z/Λ (at level 5) and (b) Ri_B (level 5 minus surface values). The vertical dashed line in the bottom panel corresponds to the critical Richardson number $Ri_B = 0.2$. The horizontal dashed lines correspond to $\mathrm{Ek} = \mathrm{Ek_{cr}} = 1$.

$$\mathrm{Ek} \equiv -\frac{\langle u'w' \rangle}{2\Omega \sin \varphi z U} \ , \tag{9}$$

where the stress and the wind speed U are measured at a height z, Ω is the Earth's angular velocity, and φ is latitude.

Figure 7 shows the Ekman number, Equation (9), measured at level 5 versus z/Λ and Ri_B. A comparison of Figures 6 and 7 defines a critical Ekman number $\mathrm{Ek_{cr}} \approx 1$, when wind veering cannot be neglected. This critical value also can be obtained from the plot of $\alpha_5 - \alpha_1$ (or $\alpha_4 - \alpha_1$) upon Ek (not shown). Thus, we conclude that in the transition regime ($\zeta \gtrsim 0.1$ and $\mathrm{Ek} \gtrsim \mathrm{Ek_{cr}} \approx 1$) the approximation of height-independent fluxes breaks down, but the effect of the Earth's rotation is still small. Therefore, $\zeta \approx 0.1$ defines the lower limit and $\mathrm{Ek} = \mathrm{Ek_{cr}} \approx 1$ can be considered as an upper limit for the transition regime.

5.3. Turbulent Ekman Layer

For more significant stability, turbulent heat flux and wind shear at the upper tower levels may be very small and approach zero. In this regime, the surface

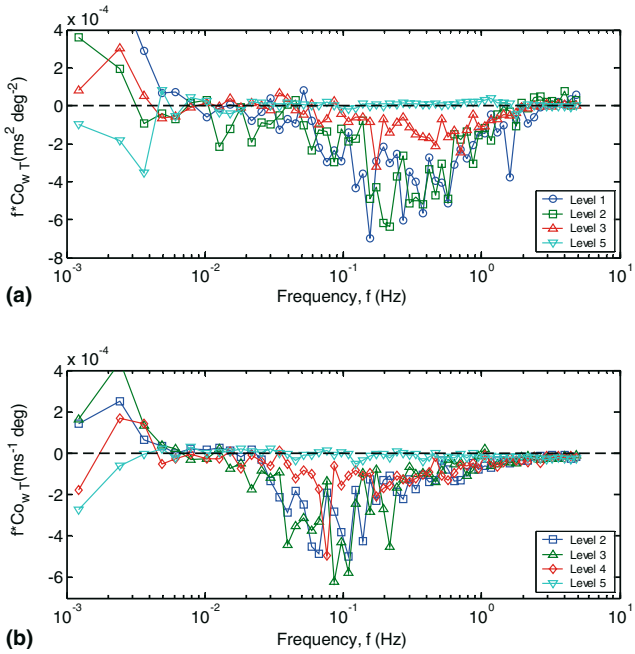

Figure 8. Typical cospectra of (a) the momentum flux at four levels (level 4 is missing), JD 355.00 (21 December, 1997) and (b) the sonic temperature flux at four levels (level 1 is missing), JD 142.75 (22 May, 1998). For data presented in the upper panel (a) the stability parameters based on the high-frequency part are $\zeta_2 \approx 3$ (level 2), $\zeta_3 \approx 10.5$ (level 3), heat flux is missing for level 1. Wind direction, α, veers with increasing height: $\alpha_1 \approx 280°$, $\alpha_2 \approx 282°$, $\alpha_3 \approx 284°$ and $\alpha_5 \approx 291°$. For data presented in the bottom panel (b) the stability parameters based on the high-frequency part increases with increasing height are $\zeta_2 \approx 1.41$, $\zeta_3 \approx 2.052$, $\zeta_4 \approx 6.336$ and $\zeta_5 \approx 8.125$ (levels 2–5 respectively). Wind direction at four levels: $\alpha_2 \approx 130°$, $\alpha_3 \approx 127°$, $\alpha_4 \approx 138°$ and $\alpha_5 \approx 162°$.

layer, where turbulence is continuous, may be very shallow, less than 5 m (cf. Smedman, 1988; King, 1990). We observed a layered structure with weak turbulence occupying the near-surface layer (usually the 2–3 lowest sonic levels) and collapsed turbulence (no turbulence) above (the upper 1 or 2 sonic levels). Typical cases of the SBL structure in this regime are shown in Figure 8 (some other examples can be found in Grachev et al., 2002). In this regime, the influence of the Coriolis effect (see the wind-direction data in the captions for Figure 8) and gravity waves comes into play. Typically there is a spectral gap and the cospectra in Figure 8 can be partitioned into turbulent (high-frequency) and non-turbulent (low-frequency) parts. We speculate that the low-frequency disturbances in Figure 8 are associated with internal gravity waves with periods of several minutes.

According to Figure 7b, there is a region where the wind is influenced by the turning effect of the Coriolis force ($\mathrm{Ek} \lesssim \mathrm{Ek}_{\mathrm{cr}} \approx 1$), the Richardson

number does not exceed its critical value ($Ri_B \lesssim Ri_{B\,cr} \approx 0.2$), and the turbulence is more or less continuous (typically $O(1) \lesssim \zeta \lesssim O(10)$ or $0.07 \lesssim Ri_B \lesssim 0.2$). Examples of this regime can be found in Figure 8a (levels 2 and 3) and Figure 8b (levels 3 and 4). Turbulence at level 5 in both Figures 8a and 8b is obviously collapsed.

According to Figures 6 and 8 (see captions to Figure 8), the turning of the wind vector averages several degrees. However, the turning angle increases drastically where frictional effects become negligible (level 5 in Figure 8); and perhaps the regime at this level is associated with an intermittently turbulent Ekman layer (see next section). Note that both the transition and the turbulent Ekman layer regimes are likely to be non-stationary since they are associated with fluxes that vary with height. Assumptions of MOST appear to break down in the turbulent Ekman layer.

As stability increases, turbulence decays and vertical fluxes vanish (e.g., Figure 1). The behaviour of the turbulent fluxes and other characteristics, including the critical Richardson number, are poorly understood in very stable conditions. This is due to the general lack of observations and to contradictory results (e.g., Mahrt, 1999). With the SHEBA data, we can consider the behaviour of τ and H_S near the critical Richardson number in more detail. Figures 9 and 10 show decaying momentum and heat fluxes as a function of the different stability parameters. The bulk Richardson number in Figure 9 is computed according to Equation (7) and the flux and gradient Richardson numbers in Figure 10 are based on Equation (6). Both the stress and the sensible heat flux decrease rapidly with increasing stability, but τ falls faster than H_S. Thus, small but still significant heat flux and negligibly small stress characterize this situation.

According to Figure 9b and d, the uw covariance falls faster than the heat flux since both u' and w' (or standard deviations σ_u and σ_w) approach zero, while T' (or σ_T) is small but still finite even in the very stable case (Grachev et al., 2003). This behaviour of σ_T may be associated with a surface that is inhomogeneous in temperature and with a strong vertical temperature gradient. Turbulence characteristics and vertical profiles of wind velocity and temperature over inhomogeneous land surface were described by Kukharets and Tsvang (1998) and Tsvang et al. (1998). Small-scale spatial variations of the surface temperature (up to several K) lead to higher values for σ_T/T_* than predicted by MOST for a uniform surface (Tsvang et al., 1998). Andreas et al. (1998) reported similar behaviour for humidity statistics over a surface with vegetation that was patchy at metre scales.

Similar effects may have been important during SHEBA. The ice floe around the ASFG main tower was multi-year pack ice with varying thickness and a surface composed of ice (of different type, salinity, etc.), snow (of different depth, age, etc.), meltponds, and even leads. These surface patches are characterized by different albedo, thermal capacity and conductivity and,

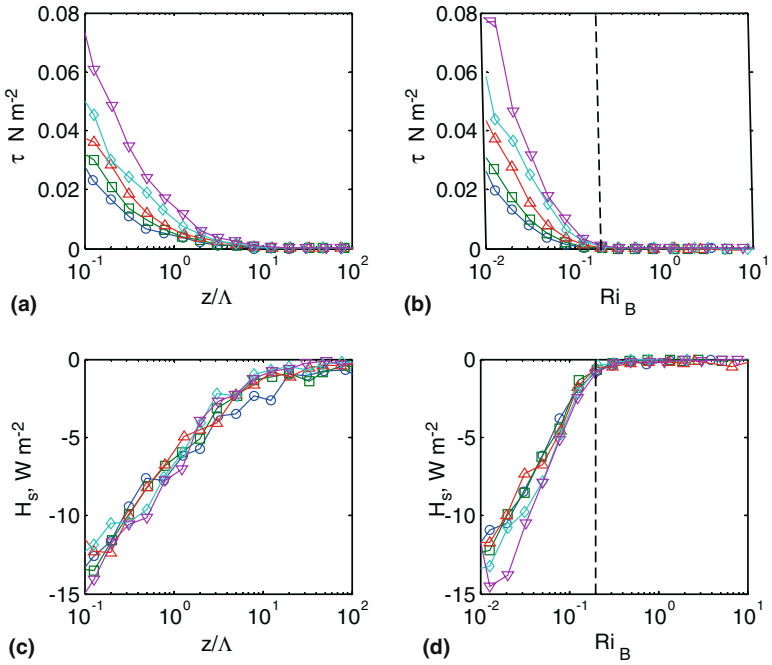

Figure 9. Behaviour of the momentum and sensible heat fluxes near the critical Richardson number computed during the 11 months of measurements: (a) τ versus z/Λ, (b) τ versus Ri_B, (c) H_S versus z/Λ and (d) H_S versus Ri_B. Vertical dashed lines correspond to $Ri_B = 0.2$. Symbols are the same as in Figure 1.

therefore, may have different temperatures. Paulson and Pegau (2001) reported that the surface temperature of the open water during the summer is about 2 °C, whereas the ice surface temperature cannot rise above 0 °C. These 'hot' and 'cold' spots generate small-scale advection (see Tsvang et al., 1998, their Figure 4) which enhances σ_T and the sensible heat flux. Though small, this contribution may be enough to cause discrepancy of the decay rates of the momentum and sensible heat fluxes in Figures 9 and 10.

One might expect that similar to flow over aerodynamically heterogeneous terrain (e.g., Goode and Belcher, 1999), there is a blending layer over a surface that is inhomogeneous in temperature. Across the blending layer the stress and the sensible heat flux adjust from their surface values to their values aloft. Thus, measurements at levels 1 and 2 may be affected by the surface inhomogeneity and even these levels may be within the blending layer, which causes departures of φ_m and φ_h (Figures 4 and 5) and Rf and Ri (Figure 10).

Note that some of the correlation between the fluxes and z/Λ and Rf (Figure 9a and c and 10a and c) may be due to self-correlation, owing to the fact that fluxes appear in both the axis variables (e.g., Mahrt et al., 1998 and

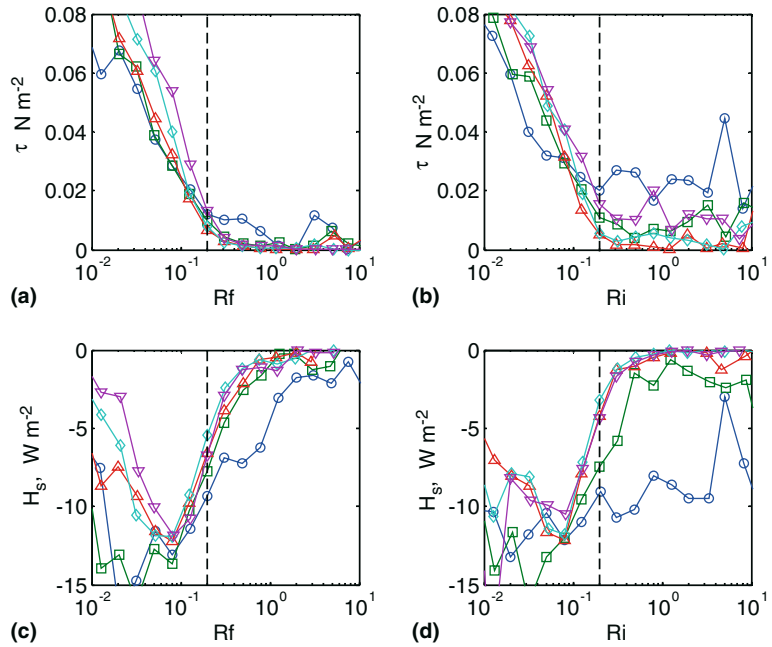

Figure 10. Same as Figure 9 but plotted (a) τ versus Rf, (b) τ versus Ri, (c) H_S versus Rf and (d) H_S versus Ri. Vertical dashed lines correspond to $Rf = 0.2$ and $Ri = 0.2$. Symbols are the same as in Figure 1.

Mahrt, 1999). However, there is no artificial correlation in the coordinates when the fluxes are plotted versus Ri_B and Ri (Figure 9b and d, 10b and d).

According to Figure 9b and d, a bulk Richardson number of about 0.2 may be considered as the critical value; that is $Ri_{B\,cr} \approx 0.2$. However, τ collapses at a value of Ri_B slightly less than 0.2, and H_S collapses at a value slightly greater than 0.2. Apparently there is no 'critical' value of z/Λ (Figure 9a and c). Andreas (2002) and Zilitinkevich and Baklanov (2002) recently reviewed the different expressions for the critical Richardson number. These surveys show that the critical Richardson number obtained in different studies varies over a wide range, e.g., $Ri_{cr} = 0.15{-}0.55$ (Zilitinkevich and Baklanov, 2002).

The flux and gradient Richardson numbers, especially for levels 1 and 2 (Figure 10), show more scatter than the bulk Richardson number (Figure 9) because of the scatter in φ_m and φ_h (cf. Figure 5) associated with the flux intermittency and the influence of a surface that is inhomogeneous in temperature. For both Rf and Ri, significant turbulent fluxes were observed when the Richardson number exceeded the commonly accepted 'critical' value 0.2 (Figure 10). The momentum flux goes to zero at about $Rf \approx Ri \approx 0.3{-}0.5$ (Figure 10a and b), whereas the sensible heat flux almost ceases at higher

values, $Rf \approx Ri \approx 0.8-1.0$ (Figure 10c and d). Furthermore, determining $\mathrm{Rf}_{\mathrm{cr}}$ is complicated by self-correlation, as discussed above. Using the fluxes is preferable to using velocity and temperature variances for studying decaying turbulence (Figures 9 and 10) since noise is not correlated in the covariances $\langle u'w' \rangle$ and $\langle w'T' \rangle$. Thus, based on the SHEBA data, we recommend the critical number $Ri_{\mathrm{B\,cr}} \approx 0.2$ for practical applications (Figures 9b and d). Obviously, this regime is bounded by the critical Ekman and Richardson numbers, $\mathrm{Ek} \lesssim \mathrm{Ek}_{\mathrm{cr}} \approx 1$ and $Ri_{\mathrm{B}} \lesssim Ri_{\mathrm{B\,cr}} \approx 0.2$.

5.4. Intermittently turbulent Ekman layer

In the SBL when $Ri_{\mathrm{B}} \gtrsim Ri_{\mathrm{B\,cr}} \approx 0.2$ ($\zeta \gtrsim \mathrm{O}(10)$), the basic state is associated with vanishing fluxes and the strong influence of the Earth's rotation. This regime can be treated as the supercritical stable regime (by definition) or the very stable regime (cf. Mahrt, 1999).

Very stable states observed during SHEBA were usually associated with light winds and clear skies during both dark and sunlit periods. Note that the presence or absence of clouds has a major impact on the near-surface Arctic winter environment (Persson et al., 2002a). During the dark period, a diurnal cycle is absent, and a residual layer, more common in the mid-latitude nocturnal SBL, typically does not form. Thus, the SBL at high latitudes can exist for prolonged periods and may not be separated from the outer (or Ekman) layer. Such situations were observed at Plateau Station in the Antarctic by Dabberdt (1970) and Lettau et al. (1977). According to their data, winter stability at Plateau was so extreme that the top of their 32-m tower was in the upper part of the planetary boundary layer. In fact, a long-lived SBL is a regular state in the Antarctic during sunless periods, and the Ekman-type spiral is observed near the surface even for monthly mean data (Dabberdt, 1970). It seems likely that the Plateau Station data include some of the most stable conditions ever observed on the Earth's surface.

The influence of the Earth's rotation on the near-surface atmospheric layer was also observed during SHEBA. Examples of the Ekman spiral for the two polar seasons are shown in Figures 11 and 12. The wind vector decays and turns clockwise with decreasing height, as expected for the Northern Hemisphere. In the case shown in Figure 11, the supercritical regime ($Ri_{\mathrm{B}} \gtrsim 0.2$), or intermittently turbulent Ekman layer, is associated with the two upper levels. The turbulent Ekman layer, therefore, occupies levels 1–3. Figure 12 shows a more extreme case when turbulence collapses at all five levels. The observed Ekman spirals show that the wind vector at level 5 rotates about 30°–50° to the right of the wind vector at level 1 (cf. Figure 8). The case shown in Figure 11 occurred during the polar night, and the observed Ekman

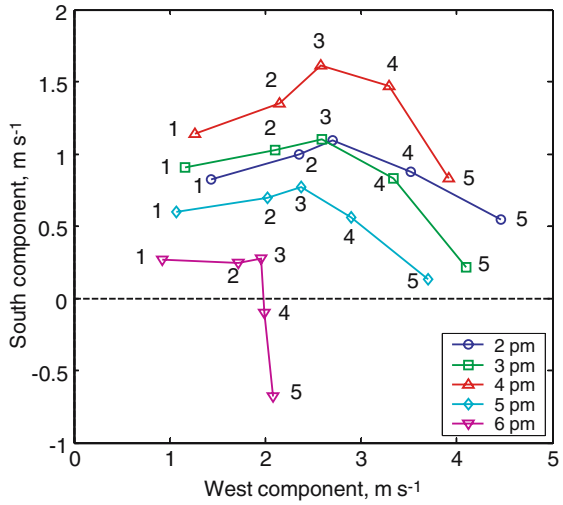

Figure 11. Evolving Ekman-type spirals during the polar night observed during JD 317–318 (13–14 November, 1997) for 5 h from 2200–0200 UTC (1400–1800 local time; see legend). Markers indicate ends of wind vectors at levels 1 to 5 (2.0, 3.1, 5.1, 8.9 and 14.9 m).

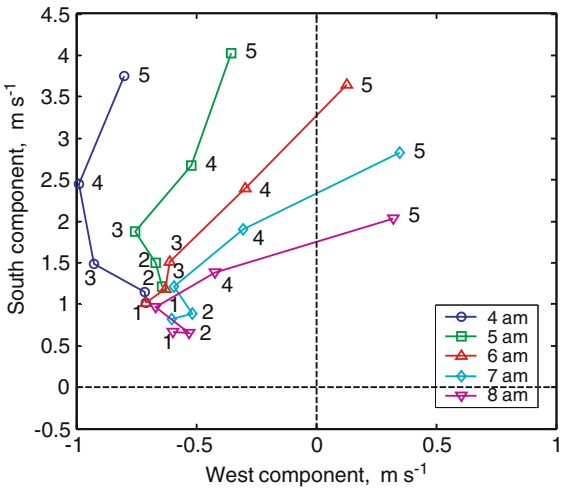

Figure 12. Evolving Ekman-type spirals during the polar day observed during JD 142 (22 May, 1998) for 5 h from 1200 to 1600 UTC (0400–0800 local time, see the legend). Markers indicate ends of wind vectors at levels 1 to 5 (1.9, 2.7, 4.7, 8.6 and 17.7 m).

spiral is more or less stationary from 1400–1700. Figure 12 shows a nonstationary Ekman layer when the wind spiral is affected by an inertial oscillation (e.g., Andreas et al., 2000).

Stationary surface wind veering was observed at Plateau Station in the Antarctic (Dabberdt, 1970; Lettau and Dabberdt, 1970; Lettau et al., 1977). Often such near-surface directional shear (wind veering) is treated solely as a manifestation of the effects of stability (e.g., Arya, 2001, Sec. 6.5). However, the opposite rotation of the wind spirals in the Northern (SHEBA) and Southern (Plateau Station) Hemispheres clearly indicates that this phenomenon is associated with the Earth's rotation.

Note that the 'classical' atmospheric Ekman layer is usually located in a region several hundred metres above the surface and extends over layers of at least 15–20 times the tower height (Van Ulden and Wieringa, 1996). The atmospheric surface Ekman layer reported here is most likely similar to the oceanic Ekman layers at the sea surface (Price et al., 1987; McPhee and Martinson, 1994) and at the bottom of the ocean caused by the strong stratification.

As mentioned above, even though $Ri_{\mathrm{B}} \gtrsim Ri_{\mathrm{B\,cr}} \approx 0.2$, some sporadic and intermittent turbulence persists in the very stable regime. According to the SHEBA data, there is no evidence that suppression of turbulence by stable stratification causes a transition to laminar flow. Figure 13 shows ratios of the turbulent viscosity, $\nu_t = -\frac{\langle u'w' \rangle}{dU/dz}$, to the molecular viscosity, ν(a), and the turbulent thermal conductivity, $k_t = -\frac{\langle w'T' \rangle}{d\theta/dz}$, to the molecular thermal conductivity, k(b). Even for $Ri_{\mathrm{B}} \approx Ri_{\mathrm{B\,cr}}$, the turbulent exchange coefficients exceed their molecular counterparts by 10^2 to 10^3 . Based on measurements at Halley Base, Antarctica, Yagüe and Cano (1994) and Yagüe et al. (2001) found that, in the supercritical regime $\nu_t \sim k_t \sim 10^{-2}$–$10^{-3}\mathrm{m^2sec^{-1}}$, which is in good agreement with our results. Thus, even in the supercritical regime ($Ri_{\mathrm{B}} \gtrsim Ri_{\mathrm{B\,cr}}$) there is no evidence of a transition to a laminar Ekman layer, as originally predicted by Ekman (1905). According to Ekman's (1905) solution, a characteristic height h_E for the spiral is $\pi\sqrt{\nu/\Omega \sin \varphi} \approx 1.4$ m, where ν is the molecular viscosity of air. There is no observational evidence for the occurrence of such a shallow laminar Ekman layer in the atmosphere. By replacing ν with the eddy viscosity (ν_t), which is about two to three orders of magnitude larger for $Ri_{\mathrm{B}} \approx Ri_{\mathrm{B\,cr}}$ (Figure 13a), we can obtain an Ekman layer depth that is realistic (≈15–45 m, Figures 11 and 12). The supercritical stable regime is described by the criteria $Ri_{\mathrm{B}} \gtrsim Ri_{\mathrm{B\,cr}} \approx 0.2$ or $\zeta \gtrsim \mathrm{O}(10)$.

Our SHEBA data shed light on the scaling laws in the limit of very strong stability. Figures 14 and 15 show the stability functions φ_{m} and φ_{h} in log–log representation covering six orders of magnitude of the stability parameter (cf. Figures 4 and 5). The data expressed in the framework of surface scaling (Figures 14a and 15a) show less scatter than those with local scaling (Figures 14b and 15b). According to Figure 14, the stability function φ_{m} has a $\zeta^{1/3}$ dependence in the very stable regime; that is, it increases more slowly than predicted by the Businger–Dyer and Beljaars–Holtslag relationships. At the

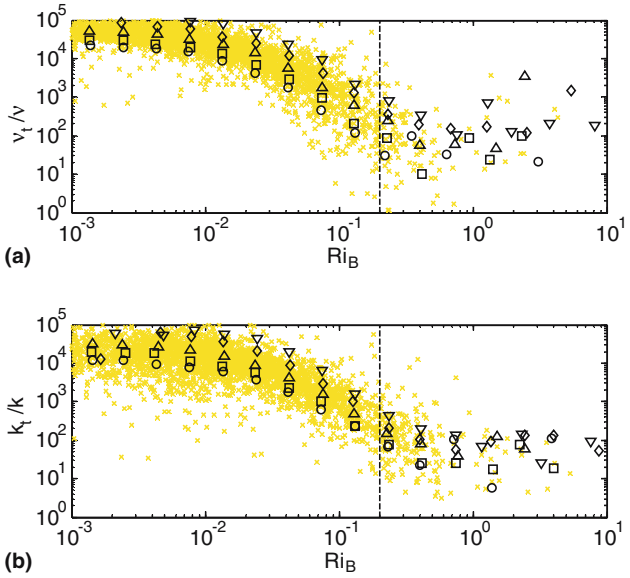

Figure 13. The bin-averaged (medians) ratio of the (a) turbulent viscosity to the molecular viscosity, ν_t/ν, and (b) turbulent thermal conductivity to the molecular thermal conductivity, k_t/k, as function of the bulk Richardson number, Ri_B. The vertical dashed lines correspond to $Ri_B = 0.2$. Individual 1-h averaged data based on the median fluxes for five levels are shown as background crosses. Symbols are the same as in Figure 4.

same time, the stability function φ_h shown in Figure 15 initially increases with increasing ζ, reaches a maximum at $\zeta \approx 10$, and then decreases with a slope close to $-1/3$ (i.e., $\varphi_h \propto \zeta^{-1/3}$). The data presented in Figures 14 and 15 demonstrate that both functions φ_m and φ_h do not follow z-less behaviour (φ_m, $\varphi_h \propto \zeta$) for very strong stability. This result confirms the conclusion of Pahlow et al. (2001) that the concept of z-less stratification is not valid in general.

The observed dependences, $\varphi_m \propto \zeta^{1/3}$ and $\varphi_h \propto \zeta^{-1/3}$, can be derived from Equation (5) if we assume that dU/dz and $d\theta/dz$ are independent of u_* for $\zeta >> 1$. The stress, or equivalently u_*, is no longer a primary scaling parameter due to the asymmetric decay of the uw and wT covariances; and the stress falls faster with stability than the heat flux. By analogy with the 'z-less' regime, we may term this limit the frictionless (or 'u_*-less') regime. Formally, the scaling relationships for the stability functions, $\varphi_m \propto \zeta^{1/3}$ and $\varphi_h \propto \zeta^{-1/3}$, and other variables (such as the variances) in the limit of very stable stratification are the same as in the limit of very unstable stratification (free convection) derived by Kader and Yaglom (1990). In both cases, when the stability parameter reaches very large values (positive or negative), $|\zeta| >> 1$, the stress becomes insignificant and u_* ceases to be a scaling

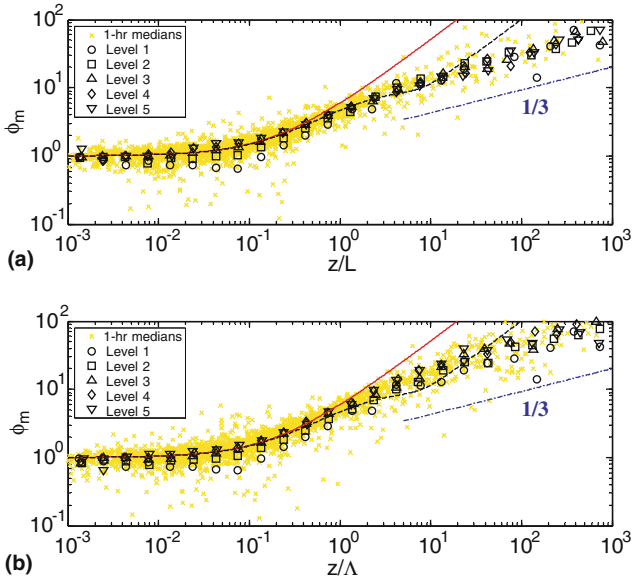

Figure 14. Plots of the bin-averaged non-dimensional velocity gradient, φ_m, in log-log coordinates against (a) the surface MOST stability parameter, z/L and (b) the local MOST stability parameter, z/Λ, during the 11 months of measurements. Notation is the same as in Figure 4.

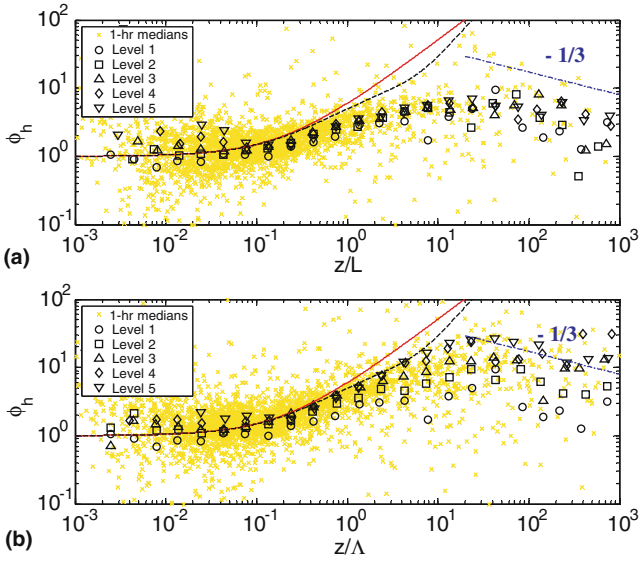

Figure 15. Same as Figure 14 but for the non-dimensional temperature gradient, φ_h.

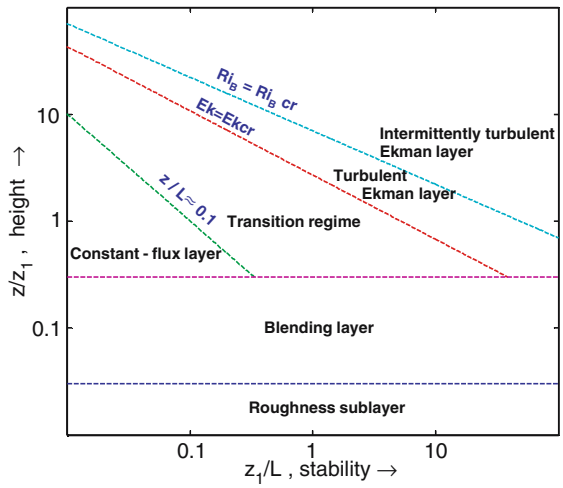

Figure 16. Schematic diagram of the SBL scaling regimes as functions of the stability and height. Here $z_1 \approx 2\,\mathrm{m}$ (level 1). Dividing lines between the scaling regions are sketched.

parameter. Although there is a formal coincidence, the physical reasons for these two limits are different. In the free-convection asymptotic limit $U \to 0$ and therefore $u_* \to 0$, while in the limit of very strong stability $U \neq 0$ and $u_* \to 0$ for the reason that vertical mixing is suppressed by the very stable stratification. Further examination of the u_*-less concept requires a separate study and is not the purpose of this paper.

Figure 16 summarizes the four scaling regimes we have identified. The SBL scaling regions are located over a roughness sublayer in the case of the homogeneous surface or over the blending layer in the case of a patchy surface that is inhomogeneous in temperature (see the discussion in Section 5.3). In this schematic diagram, the SBL regions are shown as functions of stability and height. We use the stability parameter z_1/L with fixed height $z_1 \approx 2\,\mathrm{m}$ instead of $\zeta = z/L$ or z/Λ to separate height and stability in Figure 16. Holtslag and Nieuwstadt (1986) and Sorbjan (1989), in a similar diagram for the nocturnal SBL, use z/h and h/L, where h is the mean height of the turbulent boundary layer. In Figure 16, h is defined by the line $Ri_\mathrm{B} = Ri_{\mathrm{B\,cr}} \approx 0.2$. The height to which the surface temperature inversion extends is generally greater than h, and averages 1000–1300 m during December 1997–March 1998 and 300–800 m during April November 1998 (Persson et al., 2002a; Uttal et al., 2002). A 'true' limit of very strong stability when a $d\theta/dz > 0$ and $U \equiv 0 (\zeta \to \infty)$ is not shown in Figure 16 because this is a simplified case. Such regimes is observed in sinkholes in mountain areas.

6. Conclusions

We discussed the structure of the stable boundary layer (SBL) based on tower measurements made during SHEBA. The SBL that we observed most often can be characterized as the traditional boundary layer, where turbulence is generated by surface roughness (cf. Mahrt and Vickers, 2002). We did, however, also observe the upside-down SBL and an SBL contaminated by internal gravity waves. According to our SHEBA data, stratification and the Earth's rotation control the SBL over a flat rough surface. Different SBL regimes are described in terms of the MOST stability parameter ($\zeta = z/L$), the Ekman number (Ek) that quantifies the influence of the Earth's rotation, and the bulk Richardson number (Ri_{B}) that determines the intensity of the turbulence. These three non-dimensional parameters govern four major regimes (Figure 16), which we identify as follows:

I. *Surface-layer scaling regime* (or weakly stable regime), $0 < \zeta \lesssim 0.1$. This regime is associated with shear stress and sensible heat flux that are approximately constant with height (constant-flux layer). The weakly stable boundary layer is governed by traditional MOST predictions that are valid when $\mathrm{Ek} >> 1$ and $Ri_{\mathrm{B}} << Ri_{\mathrm{B\,cr}}$.

II. *Transition regime*, $\zeta \gtrsim 0.1$ and $\mathrm{Ek} \gtrsim \mathrm{Ek_{cr}} \approx 1$ (typically $0.1 \lesssim \zeta \lesssim \mathrm{O}(1)$). In this regime, the approximation of height-independent fluxes becomes invalid. However, the flow is insensitive to the Earth's rotation and turbulence is more or less continuous ($Ri_{\mathrm{B}} < Ri_{\mathrm{B\,cr}}$). In this regime, MOST seems adequate, but similarity theory should be redefined in terms of local similarity, where the Obukhov length is based on the local fluxes at height z. In general, the stability functions, φ_{m} and φ_{h}, expressed in terms of local scaling, agree with the Businger–Dyer formulations better than those expressed in the framework of surface-layer scaling. However, φ_{m} and φ_{h} estimates based on local scaling include more scatter compared to surface-layer scaling.

III. *Turbulent Ekman layer*, $\mathrm{Ek} \lesssim \mathrm{Ek_{cr}} \approx 1$ and $Ri_{\mathrm{B}} \lesssim Ri_{\mathrm{B\,cr}} \approx 0.2$ (typically $\mathrm{O}(1) \lesssim \zeta \lesssim \mathrm{O}(10)$). In this regime, the turbulent fluxes are small and vary with height. A surface layer with continuous turbulence may be very shallow, and the wind structure is influenced by the Coriolis force. For this reason, this regime can be referred to as the turbulent Ekman layer.

IV. *Intermittently turbulent Ekman layer* (or supercritical stable regime). $Ri_{\mathrm{B}} \gtrsim Ri_{\mathrm{B\,cr}} \approx 0.2$ (typically $\zeta \gtrsim \mathrm{O}(10)$). The supercritical stable regime (or very stable case, Mahrt, 1999) is associated with collapsed turbulence ($Ri_{\mathrm{B}} \gtrsim Ri_{\mathrm{B\,cr}}$) and the strong influence of the Earth's rotation ($\mathrm{Ek} << 1$). Observed wind speeds show features of the Ekman spiral even near the surface (surface Ekman layer). The stress becomes insignificant and u_* ceases to be a relevant scaling parameter in this regime. However, even in this regime, some sporadic and intermittent turbulence persists and there is no evidence of a transition to a laminar Ekman layer on average.

The above four regimes may be considered as the basic states of the traditional SBL, though they are sometimes perturbed by gravity waves, detached elevated turbulence (upside down SBL), inertial oscillations, etc. Classifying the SBL into a few prototypes is useful way to mathematically parameterize of the very stable state. Mahrt (1999, p. 378), for example, recently emphasized the importance of the SBL parameterization for numerical modeling, especially for the very stable regime: "Virtually all models apply Monin–Obukhov similarity theory to the first model level even for very stable conditions where the surface layer does not exist or is confined to levels below the first model level. No other practical formulations exist."

According to our SHEBA data, a bulk Richardson number, Equation (7), of about 0.2 may be considered as the critical value, that is, $Ri_{\mathrm{B\,cr}} \approx 0.2$ (Figure 9). However, significant turbulent fluxes were still observed when the flux and the gradient Richardson numbers (6) exceeded the 'critical' value 0.2, Figure 10.

As the Richardson number approaches its critical value, turbulence decays and vertical fluxes vanish. However, the stress falls off faster with increasing stability than the heat flux. In other words, small but still significant heat flux (several watts per square metre) and negligibly small stress characterize this situation, which may be important for the Arctic heat budget. This asymmetric decay of the turbulent fluxes may be associated with a surface that is inhomogeneous in temperature.

Furthermore, the SHEBA data (Figures 14 and 15) demonstrate that both stability functions φ_{m} and φ_{h} do not follow the z-less behaviour (φ_{m}, $\varphi_{\mathrm{h}} \propto \zeta$) as originally predicted by Monin and Obukhov (1954) for the very strong stability (cf. Pahlow et al., 2001). However, an alternative u_*-less concept may be applied in the limit of very strong stability. According to this concept, decaying stress becomes, first, comparable with the Coriolis force ($\mathrm{Ek} \lesssim 1$) and, second, insignificant relative to the buoyancy effects ($\zeta >> 1$). The last results leads to new scaling relationships for the stability functions, $\varphi_{\mathrm{m}} \propto \zeta^{1/3}$ and $\varphi_{\mathrm{h}} \propto \zeta^{-1/3}$, which are in good agreement with the SHEBA data.

The conclusion that the Coriolis effect plays a crucial role in a very stable regime allows us to apply Ekman theory to parameterize the SBL in this case (Csanady, 1969; Price and Sundermeyer, 1999). Another important application of the Ekman approach is to model pollutant diffusion in the stable atmospheric surface layer. In the Ekman layer, the net mass transfer is to the right (left) of the wind stress in the Northern (Southern) Hemisphere.

Acknowledgements

The U.S. National Science Foundation supported this work with awards to the NOAA Environmental Technology Laboratory (OPP-97-01766), the

Cooperative Institute for Research in Environmental Sciences, University of Colorado (OPP-00-84322, OPP-00-84323), the U.S. Army Cold Regions Research and Engineering Laboratory (OPP-97-02025, OPP-00-84190), and the Naval Postgraduate School (OPP-97-01390, OPP-00-84279). The U.S. Department of the Army also supported ELA through Project 4A1611AT24. Thanks go to Jeff Hare and Jim Wilczak for suggestions on improving the manuscript.

References

Andreas, E. L: 2002, 'Parameterizing Scalar Transfer over Snow and Ice, A Review', *J. Hydrometeorol.* **3**, 417–432.

Andreas, E. L and Cash, B. A.: 1996, 'A New Formulation for the Bowen Ratio over Saturated Surfaces', *J. Appl. Meteorol.* **35**(8), 1279–1289.

Andreas, E. L, Hill, R. J., Gosz, J. R., Moore, D. I., Otto, W. D., and Sarma, A. D.: 1998, 'Statistics of Surface-Layer Turbulence over Terrain with Metre-Scale Heterogeneity', *Boundary-Layer Meteorol.* **86**, 379–408.

Andreas, E. L, Fairall, C. W., Guest, P. S., and Persson, P. O. G.: 1999, 'An Overview of the SHEBA Atmospheric Surface Flux Program', *13th Symposium on Boundary Layers and Turbulence*. Dallas, TX, Amer. Meteorol. Soc., Proceedings, 550–555.

Andreas, E. L, Claffey, K. J., and Makshtas, A. P.: 2000, 'Low-Level Atmospheric Jets and Inversions over the Western Weddell Sea', *Boundary-Layer Meteorol.* **97**, 459-486.

Andreas, E. L, Guest, P. S., Persson, P. O. G., Fairall, C. W., Horst, T. W., Moritz, R. E., and Semmer, S. R.: 2002, 'Near-Surface Water Vapor over Polar Sea Ice Is Always Near Ice-Saturation', *J. Geophys. Res.* **107**(C8), 8032, doi: 10.1029/2000JC000411.

Arya, S. P.: 2001, *Introduction to Micrometeorology*, 2nd edn., Academic Press, San Diego, 403 pp.

Beljaars, A. C. M. and Holtslag, A. A. M.: 1991, 'Flux Parameterization over Land Surfaces for Atmospheric Models', *J. Appl. Meteorol.* **30**, 327–341.

Beyrich, F.: 1997, 'Mixing Height Estimation from Sodar – A Critical Discussion', *Atm. Environ.* **21**, 3941–3953.

Businger, J. A.: 1966, 'Transfer of Heat and Momentum in the Atmospheric Boundary Layer', *Proc. Arctic Heat Budget and Atmospheric Circulation*. Santa Monica, Calif., RAND Corp., 305–332.

Businger, J. A.: 1988, 'A Note on the Businger–Dyer Profiles', *Boundary-Layer Meteorol.* **42**, 145–151.

Businger, J. A., Wyngaard, J. C., Izumi, Y., and Bradley, E. F.: 1971, 'Flux-Profile Relationships in the Atmospheric Surface Layer', *J. Atmos. Sci.* **28**, 181–189.

Claffey, K. J., Andreas, E. L, Perovich, D. K., Fairall, C. W., Guest, P. S., and Persson, P. O. G.: 1999, 'Surface Temperature Measurements at SHEBA', in *Preprint Volume, Fifth Conference on Polar Meteorology and Oceanography*, 10–15 January 1999, Dallas, TX, American Meteorological Society, Boston, pp. 327–332.

Csanady, G. T.: 1969, 'Diffusion in an Ekman Layer', *J. Atmos. Sci.* **26**(3), 414–426.

Dabberdt, W. F.: 1970, 'A Selective Climatology of Plateau Station, Antarctica', *J. Appl. Meteorol.* **9**(2), 311–315.

Derbyshire, S. H.: 1990, 'Nieuwstadt's Stable Boundary Layer Revisited', *Quart. J. Roy. Meteorol. Soc.* **116**, 127–158.

Duynkerke, P. G.: 1990, 'Turbulence, Radiation and Fog in Dutch Stable Boundary Layers', *Boundary-Layer Meteorol.* **90**(3), 447–477.

Duynkerke, P. G. and de Roode, S. R.: 2001, 'Surface Energy Balance and Turbulence Characteristics Observed at the SHEBA Ice Camp during FIRE III', *J. Geophys. Res.* **106**(D14), 15313–15322.

Dyer, A. J.: 1974, 'A Review of Flux-Profile Relationships', *Boundary-Layer Meteorol.* **7**, 363–372.

Dyer, A. J. and Bradley, E. F.: 1982, 'An Alternative Analysis of Flux-Gradient Relationships at the 1976 ITCE', *Boundary-Layer Meteorol.* **22,** 3–19.

Dyer, A. J. and Hicks, B. B.: 1970, 'Flux-Gradient Relationships in the Constant Flux Layer', *Quart. J. Roy. Meteorol. Soc.* **96**, 715–721.

Ekman, V. W.: 1905, 'On the Influence of the Earth's Rotation on Ocean Currents', *Arch. Math. Astron. Phys.* **2**, 1–52.

Forrer, J. and Rotach, M. W.: 1997, 'On the Turbulence Structure in the Stable Boundary Layer over the Greenland Ice Sheet', *Boundary-Layer Meteorol.* **85**, 111–136.

Garratt, J. R.: 1992, *The Atmospheric Boundary Layer*, Cambridge University Press, Cambridge, 316 pp.

Garratt, J. R. and Brost, R. A.: 1981, 'Radiative Cooling Effects Within and Above the Nocturnal Boundary Layer', *J. Atmos. Sci.* **38**(12), 2730–2746.

Goode, K. and Belcher, S. E.: 1999, 'On the Parameterization of the Effective Roughness Length for Momentum Transfer over Heterogeneous Terrain', *Boundary-Layer Meteorol.* **93**(1), 133–154.

Grachev, A. A., Fairall, C. W., Persson, P. O. G., Andreas, E. L, and Guest, P. S.: 2002, 'Stable Boundary-Layer Regimes Observed During the SHEBA Experiment', in *15th Symposium on Boundary Layers and Turbulence*. Wageningen, The Netherlands, Am. Meteorol. Soc., Proceedings, 374–377.

Grachev, A. A., Fairall, C. W., Persson, P. O. G., Andreas, E. L, Guest, P. S., and Jordan, R. E.: 2003, 'Turbulence Decay in the Stable Arctic Boundary Layer', *Seventh Conference on Polar Meteorology and Oceanography and Joint Symposium on High-Latitude Climate Variations*. Hyannis, Massachusetts, Am. Meteorol. Soc., Preprint CD-ROM.

Guest, P. S., Andreas, E. L, Fairall, C. W., and Persson, P. O. G.: 1999, 'Problems with Surface Layer Similarity Theory in the Arctic', *Fifth Conference on Polar Meteorology and Oceanography*. Dallas, TX, Am. Meteorol. Soc., Proceedings, 132–135.

Högström, U.: 1988, 'Non-Dimensional Wind and Temperature Profiles in the Atmospheric Surface Layer: A Re-Evaluation', *Boundary-Layer Meteorol.* **42**, 55–78.

Holtslag, A. A. M. and Nieuwstadt, F. T. M.: 1986, 'Scaling the Atmospheric Boundary Layer', *Boundary-Layer Meteorol.* **36**, 201–209.

Howell, J. F. and Sun, J.: 1999, 'Surface-Layer Fluxes in Stable Conditions', *Boundary-Layer Meteorol.* **90**(3), 495–520.

Jordan, R. E., Andreas, E. L, and Makshtas, A. P.: 1999, 'Heat Budget of Snow-Covered Sea Ice at North Pole 4', *J. Geophys. Res.* **104**, 7785–7806.

Kader, B. A. and Yaglom, A. M.: 1990, 'Mean Fields and Fluctuation Moments in Unstably Stratified Turbulent Boundary Layers', *J. Fluid Mech.* **212**, 637–662.

Kaimal, J. C. and Gaynor, J. E.: 1991, 'Another Look at Sonic Thermometry', *Boundary-Layer Meteorol.* **56**, 401–410.

Kaimal, J. C. and Finnigan, J. J.: 1994, *Atmospheric Boundary Layer Flows: Their Structure and Measurements*, Oxford University Press, New York, Oxford, 289 pp.

King, J. C.: 1990, 'Some Measurements of Turbulence over an Antarctic Shelf', *Quart. J. Roy. Meteorol. Soc.* **116**, 379–400.

Kukharets, V. P. and Tsvang, L. R.: 1998, 'Atmospheric Turbulence Characteristics over a Temperature-Inhomogeneous Land Surface. Part I: Statistical Characteristics of Small-Scale Spatial Inhomogeneities of Land Surface Temperature', *Boundary-Layer Meteorol.* **86**(1), 89–101.

Larsen, S. E., Edson, J. B., Fairall, C. W., and Mestayer, P. G.: 1993, 'Measurements of Temperature Spectra by a Sonic Anemometer', *J. Atmos. Oceanic Technol.* **10**(3), 345–354.

Lettau, H. H. and Dabberdt, W. F.: 1970, 'Variangular Wind Spirals', *Boundary-Layer Meteorol.* **1**(1), 64–79.

Lettau, H., Riordan, A., and Kuhn, M.: 1977, 'Air Temperature and Two-Dimensional Wind Profiles in the Lowest 32 Meters as a Function of Bulk Stability', in J. A. Businger (ed.), *Meteorological Studies at Plateau Station, Antarctica*. Antarctic Research Series, Vol. **25**, Am. Geophys. Union, 77–91.

Mahrt, L.: 1998, 'Stratified Atmospheric Boundary Layers and Breakdown of Models', *Theor. Comp. Fluid. Dynam.* **11**, 263–279.

Mahrt, L.: 1999, 'Stratified Atmospheric Boundary Layers', *Boundary-Layer Meteorol.* **90**(3), 375–396.

Mahrt, L. and Vickers, D.: 2002, 'Contrasting Vertical Structures of Nocturnal Boundary Layers', *Boundary-Layer Meteorol.* **105**(2), 351–363.

Mahrt, L., Sun, J., Blumen, W., Delany, T., and Oncley, S.: 1998, 'Nocturnal Boundary-Layer Regimes', *Boundary-Layer Meteorol.* **88**, 255–278.

Malhi, Y. S.: 1995, 'The Significance of the Dual Solutions for Heat Fluxes Measured by the Temperature Fluctuation Method in Stable Conditions', *Boundary-Layer Meteorol.* **74**, 389–396.

McPhee, M. G. and Martinson, D. G.: 1994, 'Turbulent Mixing Under Drifting Pack Ice in the Weddell Sea', *Science* **263**, 218–221.

Monin, A. S. and Obukhov, A. M.: 1954, 'Basic Laws Of Turbulent Mixing in the Surface Layer of the Atmosphere', *Trudy Geofiz. Inst. Acad. Nauk SSSR.* **24**(151), 163–187.

Monin, A. S. and Yaglom, A. M.: 1971, *Statistical Fluid Mechanics: Mechanics of Turbulence*, Vol. 1, MIT Press, Cambridge, Massachusetts, 769 pp.

Nieuwstadt, F. T. M.: 1984, 'The Turbulent Structure of the Stable, Nocturnal Boundary Layer', *J. Atmos. Sci.* **41**(14), 2202–2216.

Obukhov, A. M.: 1946, 'Turbulence in an Atmosphere with a Non-Uniform Temperature', *Trudy Inst. Teoret. Geophys. Akad. Nauk SSSR.* **1**, 95–115 (translation in: *Boundary-Layer Meteorol.* 1971, **2**, 7–29).

Pahlow, M., Parlange, M. B., and Porté-Agel, F.:2001, 'On Monin–Obukhov Similarity in the Stable Atmospheric Boundary Layer', *Boundary-Layer Meteorol.* **99**(2), 225–248.

Paulson, C. A. and Pegau, W. S.: 2001, 'The Summertime Thermohaline Evolution of an Arctic Lead: Heat Budget of the Surface Layer', in *Sixth Conf. on Polar Meteorology and Oceanography*, San Diego, CA, Am. Meteorol. Soc., Proceedings, pp. 271–274.

Perovich, D. K., Tucker, W. B., and Ligett, K. A.: 2002, 'Aerial Observations of the Evolution of Ice Surface Conditions during Summer', *J. Geophys. Res.*, **107**(C10), 8048, doi:10.1029/2000JC000449.

Persson, P. O. G., Uttal, T., Intrieri, J., Fairall, C. W., Andreas, E. L, and Guest, P. S.: 1999, 'Observations of Large Thermal Transitions during the Arctic Night from a Suite of Sensors at SHEBA', in *Fifth Conference on Polar Meteorology and Oceanography*. Dallas, TX, Am. Meteorol. Soc., Proceedings, pp. 306–309.

Persson, P. O. G., Bao, J. -W., and Michelson, S.: 2002a, 'Mesoscale Modeling of the Wintertime Boundary Layer Structure over the Arctic Pack Ice', in *15th Symposium on Boundary Layers and Turbulence*. Wageningen, The Netherlands, Amer. Meteorol. Soc., Proceedings, pp. 335–338.

Persson, P. O. G., Fairall, C. W., Andreas, E. L, Guest, P. S., and Perovich, D. K.: 2002b, 'Measurements near the Atmospheric Surface Flux Group Tower at SHEBA: Near-Surface Conditions and Surface Energy Budget', *J. Geophys. Res.* **107**(C10), 8045, doi: 10.1029/2000JC000705.

Price, J. F., Weller, R. A., and Schudlich, R. R.: 1987, 'Wind-Driven Ocean Currents and Ekman Transport', *Science* **238**, 1534–1538.

Price, J. F. and Sundermeyer, M. A.: 1999, 'Stratified Ekman Layers', *J. Geophys. Res.* **104**(C9), 20467–20494.

Smedman, A. -S.: 1988, 'Observations of a Multi-Level Turbulence Structure in a Very Stable Atmospheric Boundary Layer', *Boundary-Layer Meteorol.* **44**, 231–253.

Sorbjan, Z.: 1989, *Structure of the Atmospheric Boundary Layer*. Prentice-Hall, New Jersey, 317 pp.

Tsvang, L. R., Kukharets, V. P., and Perepelkin, V. G.: 1998, 'Atmospheric Turbulence Characteristics over a Temperature-Inhomogeneous Land Surface. Part II: The Effect of Small-Scale Inhomogeneities of Surface Temperature on Some Characteristics of the Atmospheric Surface Layer', *Boundary-Layer Meteorol.* **86**(1), 103–124.

Uttal, T. 27 co-authors: 2002, 'Surface Heat Budget of the Arctic Ocean', *Bull. Amer. Meteorol. Soc.* **83**(2), 255–276.

Van Ulden, A. P. and Wieringa, J.: 1996, 'Atmospheric Boundary-Layer Research at Cabauw', *Boundary-Layer Meteorol.* **78**, 39–69.

Webb, E. K.: 1970, 'Profile Relationships: The Log-Linear Range and Extension to Strong Stability', *Quart. J. Roy. Meteorol. Soc.* **96**, 67–90.

Wyngaard, J. C.: 1973, 'On Surface-Layer Turbulence', in D. A. Haugen (ed.), *Workshop on Micrometeorology*, American Meteorology Society, Boston, MA, pp. 101–149.

Wyngaard, J. C. and Cotè, O. R.: 1972, 'Cospectral Similarity in the Atmospheric Surface Layer', *Quart. J. Roy. Meteorol.* Soc. **98**, 590–603.

Yaglom, A. M.: 1977, 'Comments on Wind and Temperature Flux-Profile Relationships', *Boundary-Layer Meteorol.* **11**, 89–102.

Yagüe, C. and Cano, J.: 1994, 'The Influence of Stratification on Heat and Momentum Turbulent Transfer in Antarctica', *Boundary-Layer Meteorol.* **69**, 123–136.

Yagüe, C., Maqueda, G., and Rees, J. M.: 2001, 'Characteristics of Turbulence in the Lower Atmosphere at Halley IV Station, Antarctica', *Dyn. Atmos. Ocean.* **34**, 205–223.

Yanes, A. V.: 1962, 'Melting of Snow and Ice in the Central Arctic', *Problems Arctic Antarctic.* **11**, g-1–g-13.

Zilitinkevich, S. S.: 2002, 'Third-Order Transport Due to Internal Waves and Non-Local Turbulence in the Stably Stratified Surface Layer', *Quart. J. Roy. Meteorol. Soc.* **128**, 913–925.

Zilitinkevich, S. and Baklanov, A.: 2002, 'Calculation of the Height of the Stable Boundary Layer in Practical Applications', *Boundary-Layer Meteorol.* **105**, 389–409.

Zilitinkevich, S. and Calanca, P.: 2000, 'An Extended Similarity-Theory for the Stably Stratified Atmospheric Surface Layer', *Quart. J. Roy. Meteorol. Soc.* **126**, 1913–1923.

Zilitinkevich, S. S. and Chalikov, D. V.: 1968, 'Determining the Universal Wind-Velocity and Temperature Profiles in the Atmospheric Boundary Layer', *Izvestiya, Acad. Sci., USSR, Atmos. Oceanic Phys.* **4**(3), 165–170 (English Edition).